

MAGNETIC AND TRANSPORT PROPERTIES BASED ON TRANSITION-METAL COMPOUNDS

GUEST EDITORS: RAN ANQ, HECHANG LEI, SHOUBAO ZHANG, AND XUAN LUO





Magnetic and Transport Properties Based on Transition-Metal Compounds

Advances in Condensed Matter Physics

Magnetic and Transport Properties Based on Transition-Metal Compounds

Guest Editors: Ran Ang, Hechang Lei, Shoubao Zhang,
and Xuan Luo



Copyright © 2014 Hindawi Publishing Corporation. All rights reserved.

This is a special issue published in “Advances in Condensed Matter Physics.” All articles are open access articles distributed under the Creative Commons Attribution License, which permits unrestricted use, distribution, and reproduction in any medium, provided the original work is properly cited.

Editorial Board

Alexandre S. Alexandrov, UK

Dario Alfe, UK

Bohdan Andraka, USA

Daniel Arovas, USA

Veer P. S. Awana, India

Arun Bansil, USA

Ward Beyermann, USA

Golam M. Bhuiyan, Bangladesh

Luis L. Bonilla, Spain

Mark Bowick, USA

Gang Cao, USA

Ashok Chatterjee, India

Ram N. P. Choudhary, India

Kim Chow, Canada

Oleg Derzhko, Ukraine

Gayanath Fernando, USA

Jörg Fink, Germany

Yuri Galperin, Norway

Russell Giannetta, USA

Gabriele F. Giuliani, USA

James L. Gole, USA

Prasenjit Guptasarma, USA

Da-Ren Hang, Taiwan

M. Zahid Hasan, USA

Yurij Holovatch, Ukraine

Chia-Ren Hu, USA

David Huber, USA

Nigel E. Hussey, UK

Philippe Jacquod, USA

Jan A. Jung, Canada

Feo V. Kusmartsev, UK

Rosa Lukaszew, USA

Dmitrii Maslov, USA

Yashowanta N. Mohapatra, India

Abhijit Mookerjee, India

Victor V. Moshchalkov, Belgium

Charles Myles, USA

Vladimir A. Osipov, Russia

Rolfe Petschek, USA

S. J. Poon, USA

Ruslan Prozorov, USA

Leonid Pryadko, USA

Charles Rosenblatt, USA

Mohindar S. Seehra, USA

Sergei Sergeenkov, Brazil

Ivan Smalyukh, USA

Daniel L. Stein, USA

Michael C. Tringides, USA

Sergio E. Ulloa, USA

Attila Virosztek, Hungary

Markus R. Wagner, Germany

Gary Wysin, USA

Gongnan Xie, China

Fajun Zhang, Germany

Contents

Magnetic and Transport Properties Based on Transition-Metal Compounds, Ran Ang, Hechang Lei, Shoubao Zhang, and Xuan Luo
Volume 2014, Article ID 926071, 2 pages

Magnetic Properties of Well-Aligned ZnO Nanorod Arrays Grown by a Simple Hydrothermal Reaction, Jiangni Yun, Rui Qu, Zhiyong Zhang, and Jun Li
Volume 2014, Article ID 627975, 6 pages

Magnetism and Microstructure Characterization of Phase Transitions in a Steel, M. Güler
Volume 2014, Article ID 408607, 4 pages

Tuning of Transport and Magnetic Properties in Epitaxial $\text{LaMnO}_{3+\delta}$ Thin Films, J. Chen, L. Hu, W. J. Lu, B. Yuan, K. J. Zhang, J. M. Dai, and Y. P. Sun
Volume 2014, Article ID 218494, 5 pages

Defects Induced Room Temperature Ferromagnetism in ZnO Thin Films, Xiao Zhang, Wei Zhang, Xinghua Zhang, Xuewen Xu, Fanbin Meng, and C. C. Tang
Volume 2014, Article ID 806327, 6 pages

Aging Effect on Electrical Conductivity of Pure and Al-Doped $\text{YBa}_2\text{Cu}_3\text{O}_{7-\delta}$ Single Crystals with a Given Topology of Planar Defects, Ruslan V. Vovk, Nikolaj R. Vovk, and Oleksandr V. Dobrovolskiy
Volume 2013, Article ID 931726, 7 pages

Oxygen Defects Mediated Magnetism of Ni Doped ZnO, W. J. Liu, X. D. Tang, Z. Tang, W. Bai, and N. Y. Tang
Volume 2013, Article ID 424398, 6 pages

Transport, Magnetic, and Thermal Properties of $\text{La}_{0.7}\text{Ca}_{0.24}\text{Sr}_{0.06}\text{MnO}_3$ Single Crystal, Tejas M. Tank, Ashish Bodhaye, Ya M. Mukovskii, and Sankar P. Sanyal
Volume 2013, Article ID 305308, 4 pages

Editorial

Magnetic and Transport Properties Based on Transition-Metal Compounds

Ran Ang,¹ Hechang Lei,² Shoubao Zhang,³ and Xuan Luo⁴

¹ Key Laboratory of Materials Physics, Institute of Solid State Physics, Chinese Academy of Sciences, Hefei 230031, China

² Frontier Research Center, Materials and Structures Laboratory, Tokyo Institute of Technology, 4259 Nagatsuta, Midori, Yokohama 226-8503, Japan

³ Advanced Solid State Chemistry Laboratory, Institute for Chemical Research, Kyoto University, Gokasho, Uji, Kyoto 611-0011, Japan

⁴ Laboratory for Pohang Emergent Materials, Department of Physics, Pohang University of Science and Technology, Pohang 790-784, Republic of Korea

Correspondence should be addressed to Ran Ang; rang@issp.ac.cn

Received 20 February 2014; Accepted 20 February 2014; Published 7 May 2014

Copyright © 2014 Ran Ang et al. This is an open access article distributed under the Creative Commons Attribution License, which permits unrestricted use, distribution, and reproduction in any medium, provided the original work is properly cited.

So far, transition-metal compounds have triggered a tremendous wave of excitement in the scientific community due to their rich physical properties. It is extremely important to understand and realize the *d*-orbital state to tune the fundamental physical properties (i.e., magnetic properties and electrical and thermal transport) of transition-metal compounds as well as their applications. The selected topics and papers include the typical magnetism and transport properties; thus it is worth sharing with many readers. This special issue contains seven papers. The detailed information is as follows.

In the paper “*Tuning of transport and magnetic properties in epitaxial LaMnO_{3+δ} thin films*,” J. Chen et al. present the effect of compressive strain induced by substrate on the transport and magnetic properties of LaMnO_{3+δ} thin films. It is found that the insulator-metal transition, charge/orbital ordering transition, and paramagnetic-ferromagnetic transition are suppressed by the compressive strain. In particular, the electronic and magnetic transition temperatures decrease with increasing the compressive strain. The present results reveal that the lattice degree of freedom plays a key role to control the transport and magnetic properties of the strongly correlated LaMnO_{3+δ} thin films.

In the paper entitled “*Aging effect on electrical conductivity of pure and Al-doped YBa₂Cu₃O_{7-δ} single crystals with a given topology of planar defects*,” R. V. Vovk et al. present

the study of the conducting properties in the basal *ab* plane of pure and Al-doped YBa₂Cu₃O_{7-δ} single crystals before and after long-time exposure in air atmosphere. It is shown that prolonged aging leads to an increase of the density of effective scattering centers for the normal carriers. The aluminum doping has been revealed to partially slow down the degradation of the conducting properties in process of aging. The excess conductivity, $\Delta\sigma(T)$, has been found to obey exponential dependence in the broad temperature range $T_c < T < T^*$. In the pseudogap regime, the mean-field transition temperature T^* and the 3D-2D crossover point in the excess conductivity have been quantified. Near the critical temperature, $\Delta\sigma(T)$ is described well within the Aslamazov-Larkin theoretical model. Herewith, both aluminum doping and prolonged aging have been found to essentially expand the temperature interval of implementation of the pseudogap state, thus narrowing the linear section in the dependence $\rho_{ab}(T)$.

In the paper “*Magnetism and microstructure characterization of phase transitions in a steel*,” M. Güler presents the study of phase transitions in a low carbon steel according to the existing phases and their magnetism. Scanning electron microscope examinations showed that pure state of the steel was fully in the ferrite phase with equiaxed grains. Moreover, subsequent heat treatments on the studied steel also ensured the formation of austenite and followed pearlite

phases. Mössbauer spectroscopy of these phases appeared as a paramagnetic single-line absorption peak for the austenite phase and ferromagnetic six-line spectra for both ferrite and pearlite phases. From Mössbauer data the determined the internal magnetic fields of ferrite and pearlite phases were as 32.2 Tesla and 31.3 Tesla, respectively.

In the paper “*Defects induced room temperature ferromagnetism in ZnO thin films,*” X. Zhang et al. prepared polycrystalline ZnO thin films by the cosputtering method under different oxygen partial pressures. They found that the films deposited in pure argon gas exhibited ferromagnetism, whereas other films deposited under different oxygen partial pressures were diamagnetism. The study indicated that Zn interstitial may play an important role in triggering magnetic order in the ZnO thin films by inducing an alteration of electronic configuration.

In the paper “*Transport, magnetic, and thermal properties of $\text{La}_{0.7}\text{Ca}_{0.24}\text{Sr}_{0.06}\text{MnO}_3$ single crystal,*” T. M. Tank et al. present the transport, magnetic, and thermal properties of $\text{La}_{0.7}\text{Ca}_{0.24}\text{Sr}_{0.06}\text{MnO}_3$ single crystal. They found that the floating zone (FZ) method was most suitable for the growth of CMR manganite. This study reveals that the magnetic transition temperature increased substantially to 277 K which indicates the onset of long range ordering and large TCR values are a highly desirable goal in the context of the development of highly responsive bolometer device.

In the paper entitled “*Oxygen defects mediated magnetism of Ni doped ZnO,*” W. J. Liu et al. synthesize Ni doped ZnO nanoparticles by a solution route and they are annealed in O_2 , air, and Ar gas flow. Annealed ZnO samples show ferromagnetism. They discussed the origin of ferromagnetism based on magnetization and photoluminescence spectroscopy.

In another paper, J. Yun et al. present “*Magnetic properties of well-aligned ZnO nanorod arrays grown by a simple hydrothermal reaction.*” Well-aligned ZnO nanorod arrays with room temperature ferromagnetism were prepared by hydrothermal method. The ZnO nanorods show (002) direction with c -axis perpendicular to the substrate surface. They discussed the nature of the ferromagnetism on the term of photoluminescence spectrum and the first-principles calculations.

Acknowledgments

We would like to thank the authors for their significant contributions and patient assistance. We also warmly thank all reviewers on these papers.

*Ran Ang
Hechang Lei
Shoubao Zhang
Xuan Luo*

Research Article

Magnetic Properties of Well-Aligned ZnO Nanorod Arrays Grown by a Simple Hydrothermal Reaction

Jiangni Yun, Rui Qu, Zhiyong Zhang, and Jun Li

School of Information Science and Technology, Northwest University, Xi'an 710127, China

Correspondence should be addressed to Jiangni Yun; niniyun@nwu.edu.cn

Received 8 November 2013; Revised 23 January 2014; Accepted 31 January 2014; Published 29 April 2014

Academic Editor: Xuan Luo

Copyright © 2014 Jiangni Yun et al. This is an open access article distributed under the Creative Commons Attribution License, which permits unrestricted use, distribution, and reproduction in any medium, provided the original work is properly cited.

Well-aligned ZnO nanorod arrays with room temperature ferromagnetism were prepared on glass substrate through hydrothermal method. The as-prepared nanorod arrays were characterized by X-ray diffraction (XRD), scanning electron microscopy (SEM), energy dispersive spectroscopy (EDS), photoluminescence (PL) spectrum, and magnetization measurements. The XRD and SEM results indicated that the ZnO nanorods are with the wurtzite structure and exhibit preferential (002) orientation with *c*-axis perpendicular to the substrate surface. The PL results suggested that the possible defect in the as-prepared ZnO nanorod arrays might be V_{Zn} , O_i , or O_{Zn} . The first-principles calculations reveal that the room temperature ferromagnetism may result from the V_{Zn} defects present in the ZnO nanorod and the hybridization of the Zn 3d states with O 2p states is responsible for the half-metallic ferromagnetism in ZnO nanorod.

1. Introduction

Recently, one-dimensional (1D) ZnO nanorods have attracted great interest due to their tunable magnetic and optoelectronic properties [1–8]. Particularly, for the potential applications in the spin electronics, the investigation to grow well-aligned ZnO nanorod arrays with room temperature ferromagnetism has been an urgent task because it is a key process toward realizing nanoscale devices [9–11]. Synthesis methods, such as physical vapor deposition [12], chemical vapor deposition [13], and pulsed laser deposition [14], have been extensively used to obtain 1D well-aligned ZnO nanorod arrays. However, these vapor-phase processes fabrication techniques need vacuum condition, high energy consumption, sophisticated equipment, and rigid experimental conditions. Compared with the vapor-phase processes, the hydrothermal process is a low cost and environmentally friendly method, which is highly welcomed by numerous researchers [15–18].

In this study, well-aligned, single crystalline ZnO nanorod arrays with room temperature ferromagnetism and high packing density were achieved via a simple hydrothermal

process. A possible origin of the ferromagnetism in the prepared ZnO nanorod arrays related to the intrinsic defect is proposed.

2. Experimental Details

The procedure of the ZnO nanorod arrays prepared under hydrothermal condition consists of two steps: (a) preparation of ZnO seed-layer and (b) growth of ZnO nanorod arrays. In the first step, a layer of ZnO seed crystal was deposited on the glass substrate via sol-gel method. In detail, equal molar Zn $(CH_3COO)_2 \cdot 2H_2O$ and glycolic amide (0.35 mol/L) were solved in ethanol with stirring at 60°C for 12 h to yield a homogeneous solution. Subsequently, the precursor solution was dropped on the glass substrate, spinning at 3000 r/min for 30 s. Then the substrate was preheated in air at 80°C for 10 min. After that, the substrates were annealed at 500°C for 90 min in air to obtain a dense and transparent ZnO seed layer on the glass substrate by using an electronic furnace. In the second step, the glass substrate with a layer of ZnO seed crystal was placed into one autoclave filled with the precursor solutions of Zn $(CH_3COO)_2 \cdot 2H_2O$ (0.04 M) and

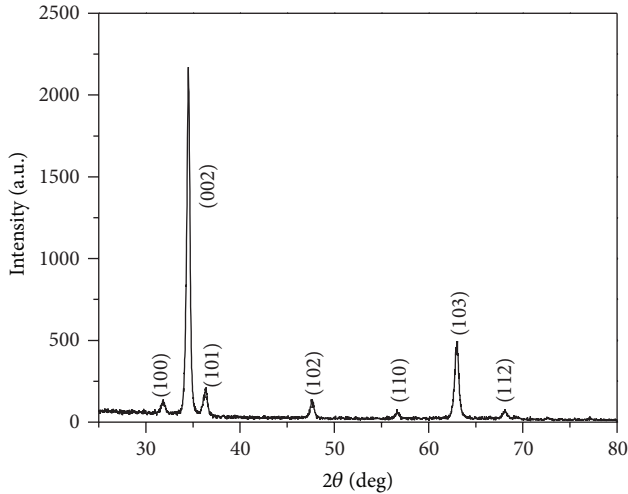


FIGURE 1: XRD pattern of the as-prepared ZnO nanorod arrays.

NaOH (0.08 M). After the autoclave is sealed safely, it is put into a bake oven at 120°C for 90 min. Finally, the glass substrate with white deposit is purged in deionized water for several times.

The obtained products are characterized by using X-ray diffraction (XRD, D/Max2550VB+/PC, Rigaku, Japan), scanning electron microscope (SEM, JSM-6390A, JEOL, Japan), photoluminescence spectrum (PL, FluoroMax-4p, HORIBA Jobin Yvon, USA), and a superconducting quantum interference device (MPMS-XL-7, Quantum Design, USA).

3. Results and Discussion

Figure 1 shows XRD pattern of the as-prepared sample. It is observed that all of the diffraction peaks can be well indexed to a wurtzite structure of ZnO. The strong and narrow diffraction peaks indicate that the material has a good crystallinity. In particular, the as-prepared sample exhibits preferential (0 0 2) orientation with *c*-axis perpendicular to the substrate surface.

Figures 2(a) and 2(b) depict the SEM images of the prepared ZnO nanorod arrays. The low-magnification SEM image in Figure 2(a) demonstrates that the nanorod array is uniform and densely packed. From the high-magnification image in Figure 2(b), it can be seen that the prepared ZnO nanorod array exhibits typical wurtzite structure and preferential (0 0 2) orientation with *c*-axis perpendicular to the substrate surface, which is reflected by the XRD pattern shown in Figure 1. Furthermore, energy dispersive spectroscopy (EDS) result indicates that the as-prepared ZnO nanorod array is only composed of Zn and O, and the atomic ratio of Zn and O is about 48.24 : 51.76. This suggests that the as-prepared nanorod arrays are nonstoichiometric and some defects may exist in the as-prepared nanorod arrays.

Figure 3 shows the room temperature PL spectra of the as-prepared ZnO nanorod arrays. A strong UV emission peak at 373 nm and three relatively weak and broad visible emissions centered at 425, 511, and 590 nm, respectively, can

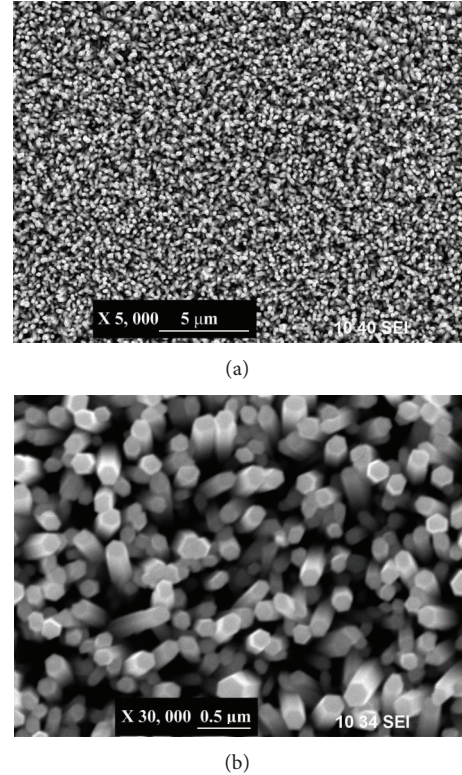


FIGURE 2: SEM images of ZnO nanorod arrays. (a) Large-scale and low magnification and (b) high magnification.

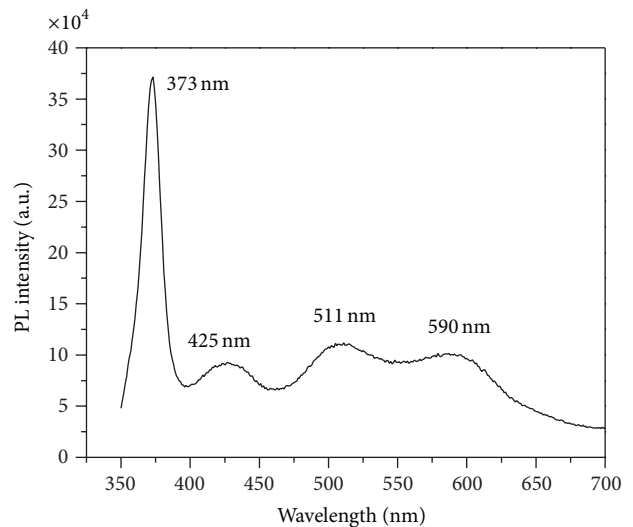


FIGURE 3: Room temperature PL spectra of the ZnO nanorod arrays.

be observed. The UV emission band is usually attributed to the near-band edge emission of the wide band gap of ZnO due to the annihilation of excitons [8, 19–21]. The visible emission is the most commonly observed and is often attributed to the defect emission [22–27]. It is known that different defects may cause different electronic structures, which will be reflected on the corresponding optical properties observed in experiments. On the other hand, the electronic structure

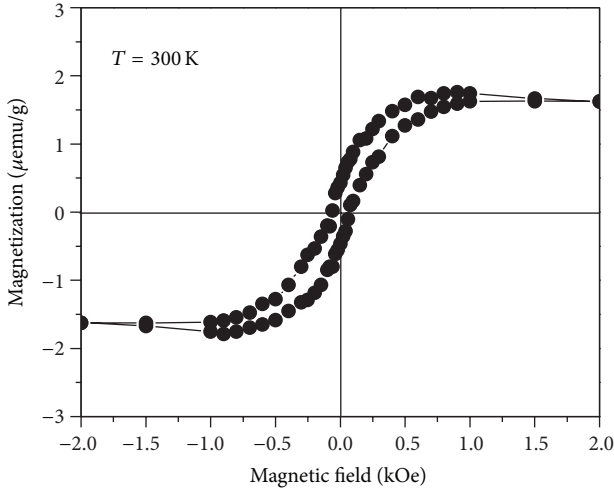


FIGURE 4: Magnetization hysteresis loops of ZnO nanorod arrays at 300 K.

of the defects can be predicted unambiguously from density functional calculations. Hence, combining the experimental observations with theoretical results may identify different defects such as oxygen vacancy (V_O), antisite oxygen (O_{Zn}), zinc vacancy (V_{Zn}), zinc interstitial (Zn_i), and oxygen interstitial (O_i) in ZnO. Theoretically, Xu et al. and Sun et al. [26, 27] calculated the electronic structure of native point defects in ZnO. Based on their results, the energy interval between the bottom of the conduction band (CB) and V_{Zn} level (3.06 eV) is approximately consistent with the energy of the blue-purple emission (425 nm, 2.92 eV) observed in our experiment. The energy interval from the bottom of the CB to the O_{Zn} level (2.38 eV) is consistent with the energy of the green emission (511 nm, 2.43 eV). The energy interval between the bottom of the CB and O_i level (2.28 eV) approximately conforms to the yellow emission (590 nm, 2.10 eV). By analysis of the experimental phenomena and the calculation of the defect levels in ZnO, we suggest that the blue emission centered at 425 nm is attributed to V_{Zn} [26, 27], the green emission centered at 511 nm originates from O_{Zn} [26, 27], and the yellow emission centered at 590 nm is related to O_i [26]. Therefore the PL results reveal that the possible defect in the as-prepared ZnO nanorod arrays might be V_{Zn} , O_i , or O_{Zn} .

Figure 4 shows the magnetization as a function of the applied field at 300 K for the as-prepared ZnO nanorod arrays. The diamagnetic contribution from the glass substrate has been subtracted from the raw data. It is interesting that the ZnO nanorod arrays exhibit room temperature ferromagnetism. The saturation magnetization M_s and remanent magnetization M_r are about 1.7×10^{-3} and 4.33×10^{-4} emu/g, respectively. The coercivity H_c is about 60 Oe. As we know, neither doping nor evidence of secondary phase exit in the as-prepared ZnO nanorod arrays; the observed room temperature ferromagnetism in the as-prepared ZnO nanorod arrays probably results from the intrinsic defect.

In order to provide more insight into this issue, we employed first-principles calculation [28] on the electronic structure and magnetic properties for the ZnO nanorod.

Since the PL study results reveal that the possible defect in the as-prepared ZnO nanorod arrays might be V_{Zn} , O_i , or O_{Zn} , thus, in the present calculations, the ZnO nanorods with V_{Zn} , O_i , or O_{Zn} defect are investigated. The wurtzite supercell containing 96 atoms is used for calculation. For the ZnO nanorod with V_{Zn} or O_{Zn} defect, there are three inequivalent defect positions, which are denoted as V_{Zn1} - V_{Zn3} and O_{Zn1} - O_{Zn3} , as shown in Figures 5(a) and 5(b). However, there are two inequivalent O_i defect positions, which are denoted as O_{i1} and O_{i2} as shown in Figure 5(c). The formation energy of V_{Zn} at V_{Zn2} site is about 0.12 and 0.38 eV smaller than that at the V_{Zn1} and V_{Zn3} sites, respectively, and, thus, V_{Zn2} is the most stable site for V_{Zn} defect. Similar to V_{Zn} , O_{Zn} also prefers at the O_{Zn2} site. While for the O_i defect, it prefers at the O_{i1} site. Therefore, the magnetic properties of ZnO nanorod with V_{Zn} , O_{Zn} , and O_i are calculated based on the V_{Zn2} , O_{Zn2} , and O_{i1} geometries, respectively.

The calculated densities of states (DOSs) for the ZnO nanorod with V_{Zn} , O_i , or O_{Zn} defect are shown in Figure 6. It is clear that the spin-up and spin-down DOSs of pure ZnO nanorod are completely symmetrical, indicating that the pure ZnO nanorod is nonmagnetic. Similarly, the ZnO nanorod with O_i or O_{Zn} defect also exhibits nonmagnetic properties. As for the ZnO nanorod with V_{Zn} defect, however, a strong spin splitting phenomenon is observed. The Fermi level passes through the band gap in the spin-down DOS and an energy gap of about 1.47 eV exists in the spin-up DOS. This demonstrates that the ZnO nanorod with V_{Zn} behaves as half-metallic.

By analysis of the partial densities of states (PDOSs) in Figure 7, it can be found that the metallic spin-down DOS near the Fermi level is mainly composed of Zn 3d and O 2p states. In particular, O 2p states make significant contribution to the magnetic moment. This suggests that the appearance of the half-metallic ferromagnetism in ZnO nanorod with V_{Zn} originates from the hybridization of the Zn 3d states with O 2p states.

4. Conclusions

In conclusion, ZnO nanorod arrays with room temperature ferromagnetism were prepared on glass substrate through hydrothermal method. The as-prepared sample shows preferential (0 0 2) orientation with c -axis perpendicular to the substrate surface. The room temperature PL measurements exhibit a prominent UV peak at about 373 nm which is attributed to the annihilation of excitons. Three relatively weak and broad visible emissions resulting from the defects can also be observed in the PL spectrum. By analysis of the calculated electronic structure of the ZnO nanorod with defects, we can get the conclusion that the V_{Zn} defects present in the ZnO nanorods are responsible for the room temperature ferromagnetism.

Conflict of Interests

The authors declare that there is no conflict of interests regarding the publication of this paper.

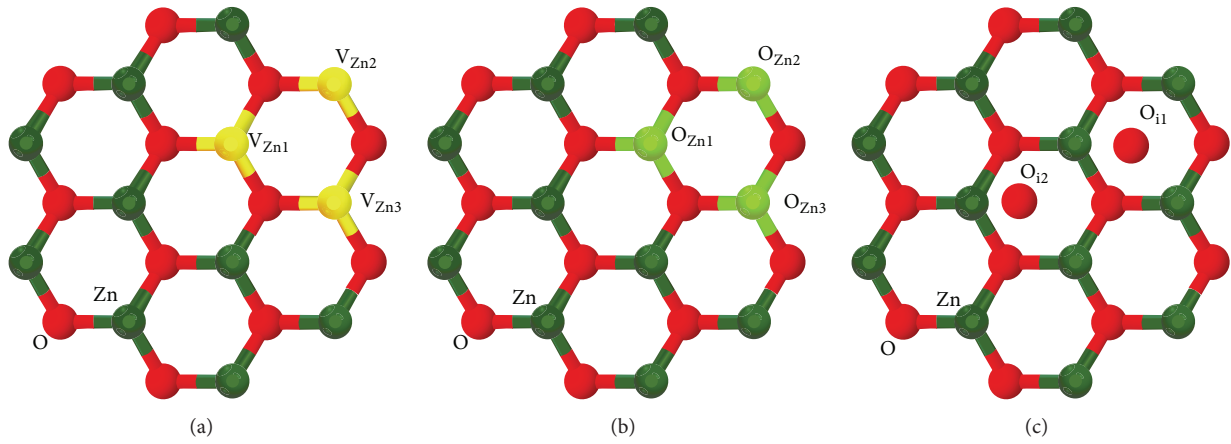


FIGURE 5: The structure of ZnO nanorods (a) with V_{Zn} , (b) with O_i , and (c) with O_{Zn} defect.

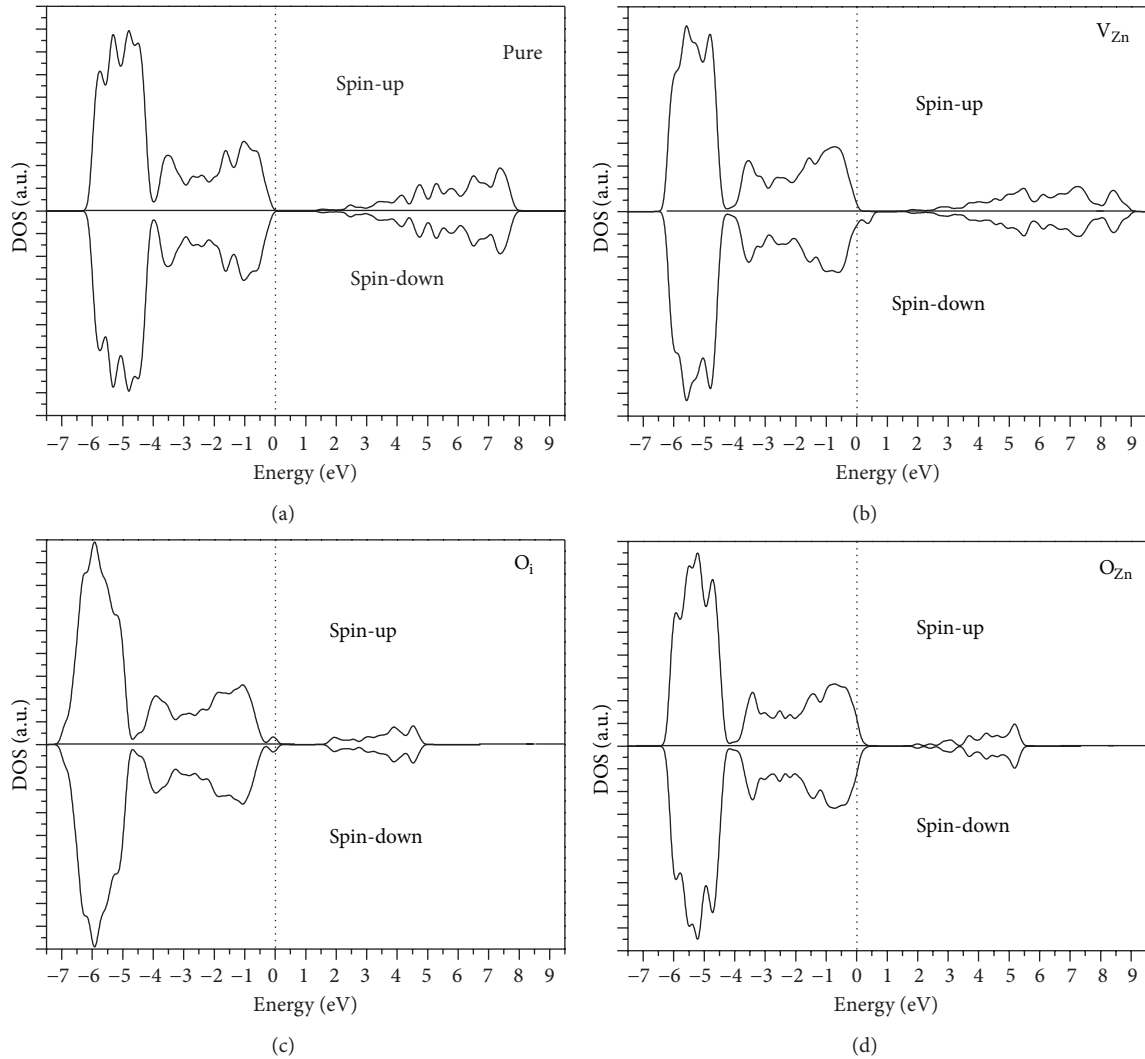


FIGURE 6: Calculated DOSs for ZnO nanorod. The Fermi level is set to zero on the energy scale, which will be adopted below unless otherwise stated.

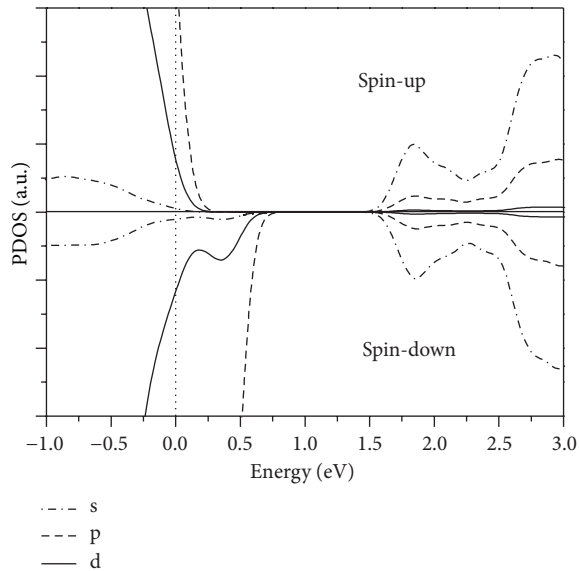


FIGURE 7: Calculated PDOS for ZnO nanorod with V_{Zn} defect.

Acknowledgments

This work is supported by the Natural Science Basic Research Plan in Shaanxi Province of China (Program nos. 2011JQ8034 and 2013KJXX-24), the Open Foundation of Key Laboratory of Photoelectronic Technology of Shaanxi Province (Grant no. ZS11009), the Science Foundation of Northwest University (nos. 10NW08 and PR10069), and the NWU Graduate Innovation and Creativity Funds (09YZZ64). The authors are also thankful for the support of the Scientific Research Program funded by the Shaanxi Provincial Education Department (Program no. 11JK0831).

References

- [1] W. Wu, G. Hu, S. Cui, Y. Zhou, and H. Wu, "Epitaxy of vertical ZnO nanorod arrays on highly (001)-oriented ZnO seed monolayer by a hydrothermal route," *Crystal Growth and Design*, vol. 8, no. 11, pp. 4014–4020, 2008.
- [2] J. T. Chen, J. Wang, R. F. Zhuo et al., "The effect of Al doping on the morphology and optical property of ZnO nanostructures prepared by hydrothermal process," *Applied Surface Science*, vol. 255, no. 7, pp. 3959–3964, 2009.
- [3] Z. Y. Wang, B. Huang, X. Qin et al., "Growth of high transmittance vertical aligned ZnO nanorod arrays with polyvinyl alcohol by hydrothermal method," *Materials Letters*, vol. 63, no. 1, pp. 130–132, 2009.
- [4] T. G. You, J. Yan, Z. Zhang et al., "Fabrication and optical properties of needle-like ZnO array by a simple hydrothermal process," *Materials Letters*, vol. 66, no. 1, pp. 246–249, 2011.
- [5] S. Ilican, "Effect of Na doping on the microstructures and optical properties of ZnO nanorods," *Journal of Alloys and Compounds*, vol. 553, pp. 225–232, 2013.
- [6] M. Guo, P. Diao, and S. Cai, "Hydrothermal growth of well-aligned ZnO nanorod arrays: dependence of morphology and alignment ordering upon preparing conditions," *Journal of Solid State Chemistry*, vol. 178, no. 6, pp. 1864–1873, 2005.
- [7] Z. Li, X. Huang, J. Liu, Y. Li, X. Ji, and G. Li, "Growth and comparison of different morphologic ZnO nanorod arrays by a simple aqueous solution route," *Materials Letters*, vol. 61, no. 22, pp. 4362–4365, 2007.
- [8] M. H. Huang, S. Mao, H. Feick et al., "Room-temperature ultraviolet nanowire nanolasers," *Science*, vol. 292, no. 5523, pp. 1897–1899, 2001.
- [9] Y. Lee, Y. Zhang, S. L. G. Ng, F. C. Kartawidjaja, and J. Wang, "Hydrothermal growth of vertical ZnO nanorods," *Journal of the American Ceramic Society*, vol. 92, no. 9, pp. 1940–1945, 2009.
- [10] H. L. Yan, X. L. Zhong, J. B. Wang et al., "Cathodoluminescence and room temperature ferromagnetism of Mn-doped ZnO nanorod arrays grown by chemical vapor deposition," *Applied Physics Letters*, vol. 90, no. 8, Article ID 082503, 2007.
- [11] A. B. Djurić, A. M. C. Ng, and X. Y. Chen, "ZnO nanostructures for optoelectronics: material properties and device applications," *Progress in Quantum Electronics*, vol. 34, no. 4, pp. 191–259, 2010.
- [12] E. Oh, S.-H. Jung, K.-H. Lee, S.-H. Jeong, S. Yu, and S. J. Rhee, "Vertically aligned Fe-doped ZnO nanorod arrays by ultrasonic irradiation and their photoluminescence properties," *Materials Letters*, vol. 62, no. 19, pp. 3456–3458, 2008.
- [13] J. Wu, S. Liu, and M. Yang, "Room-temperature ferromagnetism in well-aligned $Zn_{1-x}Co_xO$ nanorods," *Applied Physics Letters*, vol. 85, no. 6, pp. 1027–1029, 2004.
- [14] J. J. Chen, M. H. Yu, W. L. Zhou, K. Sun, and L. M. Wang, "Room-temperature ferromagnetic Co-doped ZnO nanoneedle array prepared by pulsed laser deposition," *Applied Physics Letters*, vol. 87, no. 17, p. 173119, 2005.
- [15] J. Xu, Y. P. Chen, D. Y. Chen, and J. N. Shen, "Hydrothermal synthesis and gas sensing characters of ZnO nanorods," *Sensors and Actuators B: Chemical*, vol. 113, no. 1, pp. 526–531, 2006.
- [16] S. Kumar, Y. J. Kim, B. H. Koo et al., "Room temperature ferromagnetism in chemically synthesized ZnO rods," *Materials Letters*, vol. 63, no. 2, pp. 194–196, 2009.
- [17] L. Z. Pei, H. S. Zhao, W. Tan et al., "Hydrothermal oxidation preparation of ZnO nanorods on zinc substrate," *Physica E: Low-Dimensional Systems and Nanostructures*, vol. 42, no. 5, pp. 1333–1337, 2010.
- [18] A. Aravind, M. K. Jayaraj, M. Kumar, and R. Chandra, "Optical and magnetic properties of copper doped ZnO nanorods prepared by hydrothermal method," *Journal of Materials Science: Materials in Electronics*, vol. 24, no. 1, pp. 106–112, 2013.
- [19] H. G. Kim, D. W. Hwang, and J. S. Lee, "An undoped, single-phase oxide photocatalyst working under visible light," *Journal of the American Chemical Society*, vol. 126, no. 29, pp. 8912–8913, 2004.
- [20] R. Elilarassi and G. Chandrasekaran, "Structural, optical and magnetic properties of nanoparticles of ZnO:Ni—DMS prepared by sol-gel method," *Materials Chemistry and Physics*, vol. 123, no. 2–3, pp. 450–455, 2010.
- [21] K. H. Tam, C. K. Cheung, Y. H. Leung et al., "Defects in ZnO Nanorods Prepared by a Hydrothermal Method," *The Journal of Physical Chemistry B*, vol. 110, no. 42, pp. 20865–20871, 2006.
- [22] F. Ahmed, S. Kumar, N. Arshi, M. S. Anwar, B. H. Koo, and C. G. Lee, "Defect induced room temperature ferromagnetism in well-aligned ZnO nanorods grown on Si (100) substrate," *Thin Solid Films*, vol. 519, no. 23, pp. 8199–8202, 2011.
- [23] Q. X. Zhao, P. Klason, and M. Willander, "Deep-level emissions influenced by O and Zn implantations in ZnO," *Applied Physics Letters*, vol. 87, no. 21, p. 211912, 2005.

- [24] A. F. Kohan, G. Ceder, D. Morgan, and C. G. van de Walle, "First-principles study of native point defects in ZnO," *Physical Review B—Condensed Matter and Materials Physics*, vol. 61, no. 22, pp. 15019–15027, 2000.
- [25] A. B. Djurišić and Y. H. Leung, "Optical properties of ZnO nanostructures," *Small*, vol. 2, no. 8-9, pp. 944–961, 2006.
- [26] P. S. Xu, Y. M. Sun, C. S. Shi, F. Q. Xu, and H. B. Pan, "The electronic structure and spectral properties of ZnO and its defects," *Nuclear Instruments and Methods in Physics Research B: Beam Interactions with Materials and Atoms*, vol. 199, pp. 286–290, 2003.
- [27] Y. M. Sun, *FP-LMTO study on the electronic structure of ZnO and its defects [Ph.D. dissertation]*, University of Science and Technology of China, 2000.
- [28] M. D. Segall, P. J. D. Lindan, M. J. Probert et al., "First-principles simulation: ideas, illustrations and the CASTEP code," *Journal of Physics Condensed Matter*, vol. 14, no. 11, pp. 2717–2744, 2002.

Research Article

Magnetism and Microstructure Characterization of Phase Transitions in a Steel

M. Güler

Department of Physics, Hitit University, 19030 Corum, Turkey

Correspondence should be addressed to M. Güler; mlkgnr@gmail.com

Received 30 December 2013; Accepted 25 January 2014; Published 4 March 2014

Academic Editor: Hechang Lei

Copyright © 2014 M. Güler. This is an open access article distributed under the Creative Commons Attribution License, which permits unrestricted use, distribution, and reproduction in any medium, provided the original work is properly cited.

We present phase transitions in a low carbon steel according to existing phases and their magnetism. Scanning electron microscope employed research to clarify and evaluate the microstructural details. Additionally, we utilized from Mössbauer spectroscopy for magnetic characteristics of different existed phases. Scanning electron microscope examinations showed that the pure state of the steel was fully in the ferrite phase with equiaxed grains. Moreover, subsequent heat treatments on the studied steel also ensured the first austenite and then pearlite phase formation. Mössbauer spectroscopy of these phases appeared as a paramagnetic single-line absorption peak for the austenite phase and ferromagnetic six-line spectra for both ferrite and pearlite phases. From Mössbauer data, we determined that the internal magnetic fields of ferrite and pearlite phases were as 32.2 Tesla and 31.3 Tesla, respectively.

1. Introduction

Because of their significant usage in technology and industry, detailed examinations on the solid-state phase transformations in steel drew a remarkable attention through the last century [1–3]. Applicable findings of these previous studies make steel more able to adapt quickly changing demands on daily life. Therefore, steel is the most handy and inexpensive of all materials with more than a billion tons of yearly consumption.

Steels are mainly divided into three essential categories according to their carbon content. The first category represents low carbon steel and contains maximum 0.2% C. Second category covers the medium carbon steel with 0.2% C–0.5% C. The third category represents the high carbon steel and includes more than 0.5% C or higher carbon content [4]. It should be emphasized here that low carbon steel accommodates the highest tonnage of all steel in a given year. Structural steel for buildings and bridges, line pipes, and automotive sheet applications; those are just a few major applications for low carbon steel. Also, the characteristics of all steel types depend on their chemical compositions, preparation history, applied heat treatment behaviors, and following quenching media. All of these facts on steel cause

formation of various product phases such as pearlite, bainite, and martensite [3, 5–10]. For instance, when low carbon steel cools from the austenitic region after appropriate heat treatment temperature, different percentages of austenite phase transform into a new phase including lamellar plates of ferrite and cementite (Fe_3C). On the one hand, Bain introduced this newly existing phase as “pearlite.” On the other hand, according to their formation temperatures, pearlite phase occurs between 550°C and 720°C in steel, whereas austenitic region lies between 910°C and 1535°C for ferrous alloys and steel [11].

From a physical outlook, the magnetic properties of steel are ultimately linked with their own microstructure, chemical atomic composition, and alloying conditions. When compared with each other, austenite phase is nonmagnetic while ferrite, pearlite, and bainite phases are magnetic. Noteworthy to mention here, Mössbauer spectroscopy is an accurate spectroscopic technique, which clarifies the internal magnetism (B_{int}) and volume fractions of distinct phases in steel and alloys [12–14].

Investigations on the parent austenite decomposition into product phases such as pearlite, bainite, and martensite play a particular key role during the ferrous alloy and steel production. So, the physical properties, such as transformation

TABLE 1: Applied heat treatments and following quench cases.

Specimen	Applied heat treatment
A	As in received pure state
B	1100°C → 1 h → water quenching
C	1100°C → 1 h → air cooling

kinetics, morphology, and crystallography of both ferrous alloys and steel, need extensive examinations. Interpreting of these objectives allows improving the quality and applicability of steel for many industry fields.

Literature up to date especially deals with many studies about the mechanical properties of low carbon steel. However, there is still some scarcity especially on the microstructure-magnetism relation in low carbon steel. Therefore, the focus of the current study was to examine and clarify the microstructure-magnetism relation of the different phase formations in low carbon steel after various heat treatment conditions.

2. Experimental

AISI (American Iron and Steel Institute) 1117 type commercial low carbon steel was examined in the present study. The chemical composition of this steel was as Fe-0.11% Cr-0.19% C-1.14% Mn-0.19% Si-0.02% P-0.01% Ni (wt%). The bulk sample of the steel was in the form of the cylindrical bar with 10 cm in length and 1 cm in diameter.

To reveal the microstructural details, three slabs were cut mechanically from the bulk cylindrical sample of the steel. They then were thinned to 150 μm thickness. We selected a pure slab of the steel (specimen A) to discover the microstructural details without any treatment. Afterwards, second slab (specimen B) was homogenized at 1100°C for 1 h in a quartz tube. This tube subsequently quenched into water at room temperature by cracking the quartz tube. The new third slab was homogenized at 1100°C for 1 h in a quartz tube and finally cooled in air at room temperature (specimen C) to compare the quenching media influence on specimen B. Moreover, Table 1 lists the applied heat treatments of studied specimens.

Following the applied heat treatments and quenching procedure, specimens A, B, and C were mechanically thinned to 50 μm with abrasive SiC papers. After grinding, all specimens were polished with a 3 μ diamond paste through a conventional procedure and these thin foil samples were finally etched in 3% Nital for SEM observations. A JEOL JSM 5600 type electron microscope was employed to research for the microstructural examinations under 20 kV operating voltage.

Specimens examined by SEM were used for Mössbauer spectroscopy measurements. During magnetic analysis, a Mössbauer spectrometer was performed at room temperature with a 50mCi ^{57}Co radioactive source spread in Rh. Mössbauer spectra of all measured specimens were calibrated with respect to α -Fe and isomer shift values were given to the center of the α -Fe.

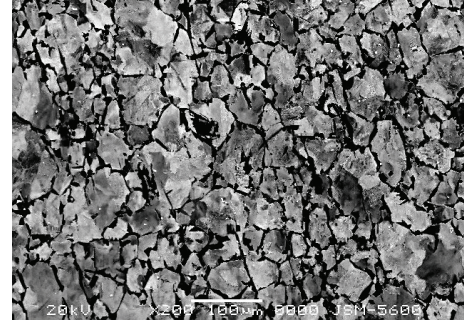


FIGURE 1: SEM micrograph of specimen A.

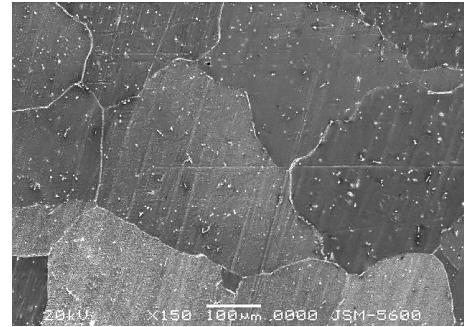


FIGURE 2: SEM micrograph of specimen B.

3. Results and Discussion

Figure 1 is a SEM micrograph taken from the specimen A. As it is obvious in Figure 1, the surface details of specimen exhibits a typical ferrite phase with the specific equiaxed grains for the pure (received) state of the steel. This phase describes the magnetic solid solution of carbon and consists of the most common microconstituent in steel. This magnetic phase appears after casting of steel, which have carbon contents lower than 0.8% [15].

Figure 2 corresponds to the SEM micrograph of B specimen. Fast cooling by water quenching caused austenite phase formation in this specimen. Further, the microstructure in Figure 2 displays the austenite phase of studied steel with typical austenite grains and grain boundaries. As well, the austenite phase forms the nonmagnetic carbon solid solution of iron. In addition, austenitic microstructures in steel are preferable because of their wide applications and uses in cutlery, hospital, and food service equipment and in tableware.

Figure 3 stands for the SEM micrograph of specimen C. Slow cooling in air at room temperature caused to coarse pearlite phase formation in C specimen with a lamellar morphology. Pearlite phase in steel forms with two prominent morphologies, namely, as coarse pearlite and fine pearlite. At low temperatures, nucleation step of phase transformation rapidly occurs and depresses the grain growth. Decreasing in the grain growth leads to fine-grained microstructure as fine pearlite. On the other hand, at higher temperatures, diffusion of the alloying ingredients allows the larger grain growth and leads to form coarse-grained microstructure as coarse

TABLE 2: Determined Mössbauer parameters of specimens A, B, and C.

Specimen	Observed phase	Volume fraction (%)	Isomer shift (mm/s)	B_{int} (Tesla)
A	Ferrite	100	0.22	32.2
B	Austenite	100	0.19	—
C	Austenite + Pearlite	12 + 88	0.18	31.3

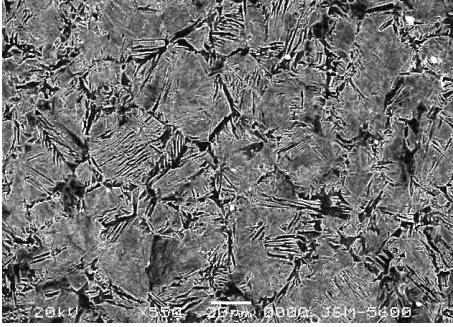


FIGURE 3: SEM micrograph of specimen C.

pearlite [16–18]. In this research, specimen C of examined low carbon steel shows a typical coarse pearlite phase as in Figure 3.

From a magnetic perspective, despite the paramagnetic ordering of the parent austenite phase, product phases such as bainite, pearlite, and martensite can exhibit ferromagnetic ordering [19]. In Mössbauer spectroscopy, a single-line accompanies the paramagnetic austenite phase, whereas the product ferromagnetic phases appear with typical sextet in the spectra [8]. Figures 4, 5, and 6 show the Mössbauer spectra with the count rates versus relative velocity plots of specimens A, B, and C, respectively. Detected ferrite phase in A specimen appears with a ferromagnetic sextet in the Mössbauer spectrum as in Figure 4. Also, Figure 5 shows a paramagnetic austenite phase singlet for specimen B. Conversely, the peaks in Figure 6 indicate both paramagnetic singlet for retained austenite phase and a ferromagnetic sextet belonging to pearlite phase in specimen C. In addition, Table 2 shows some important Mössbauer data collected from all studied specimens. The volume % transformations, internal magnetic field values, and isomer shifts of each specimen can be easily seen in Table 2.

4. Conclusions

From the determined results of present experiments, we deduced and outlined the following findings.

- (i) Present low carbon steel showed a ferritic microstructure (Figure 1) as in the received pure state. Further, different quenching media at constant homogenization temperature caused various phases in the studied steel. Rapid water quenching of the studied steel caused the austenite phase formation in specimen B (Figure 2), whereas slow air-cooling at room temperature caused coarse pearlite phase (Figure 3) formation in the specimen C.

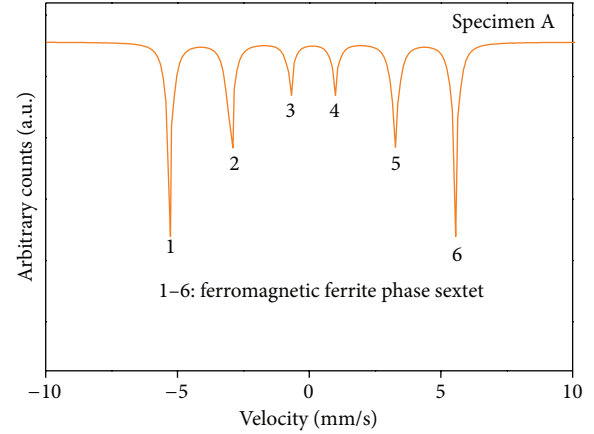


FIGURE 4: Mössbauer spectrum of specimen A.

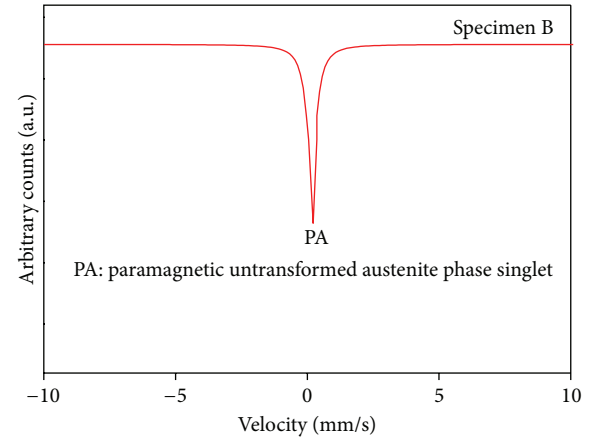


FIGURE 5: Mössbauer spectrum of specimen B.

- (ii) Depending mainly on the steel composition and applied prior heat treatment, pearlite phase displays two common morphologies in steel as fine pearlite and coarse pearlite. We observed the coarse pearlite formation (Figure 3) in the studied steel for the present composition and heat treatment.
- (iii) Determined magnetism of ferrite (Figure 4) and pearlite phases (Figure 6) explain the internal magnetic field of ferrite phase is 32.2 Tesla, and it is higher than the magnetism of pearlite phase, which has the value of 31.3 Tesla.

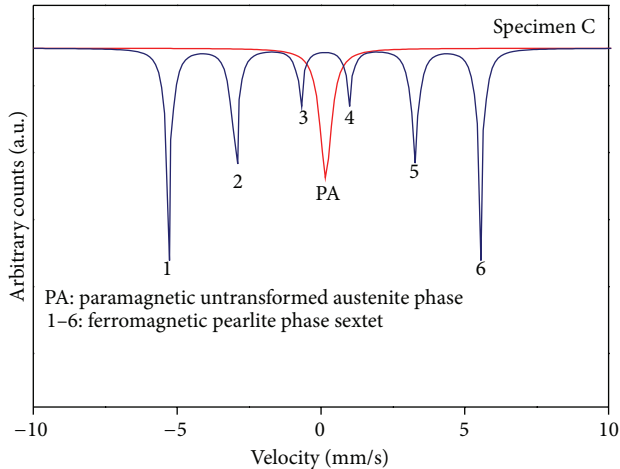


FIGURE 6: Mössbauer spectra of specimen C.

Conflict of Interests

The author declares that there is no conflict of interests regarding the publication of this paper.

References

- [1] E. C. Bain and H. W. Paxton, *Alloying Elements in Steel*, American Society for Metals, Metals Park, Ohio, USA, 2nd edition, 1966.
- [2] H. K. D. H. Bhadeshia and R. W. K. Honeycombe, *Steels, Microstructure and Properties*, Elsevier, San Diego, Calif, USA, 2006.
- [3] H. K. D. H. Bhadeshia, "Alternatives to the ferrite-pearlite microstructures," *Materials Science Forum*, vol. 284–286, pp. 39–50, 1998.
- [4] W. D. Callister, *Materials Science and Engineering*, John Wiley & Sons, New York, NY, USA, 6th edition, 2003.
- [5] A. M. Elwazri, P. Wanjara, and S. Yue, "The effect of microstructural characteristics of pearlite on the mechanical properties of hypereutectoid steel," *Materials Science and Engineering A*, vol. 404, no. 1-2, pp. 91–98, 2005.
- [6] E. Güler and M. Güler, "Deformation induced martensite characterization in Fe-30%Ni-5%Cu alloy," *Journal of Mining and Metallurgy B*, vol. 48, no. 2, pp. 259–264, 2012.
- [7] E. Güler and H. Aktaş, "Mössbauer studies on an AISI 1137 type steel," *Bulletin of Materials Science*, vol. 29, no. 3, pp. 303–306, 2006.
- [8] M. Güner, E. Güler, and H. Aktaş, "Effect of homogenization temperature on the martensitic transformation kinetics in a Fe-32%Ni-0.4%Cr alloy," *Materials Characterization*, vol. 59, no. 4, pp. 498–502, 2008.
- [9] M. Güler, E. Güler, and N. Kahveci, "Aspects of thermal martensite in a FeNiMnCo alloy," *Micron*, vol. 41, no. 5, pp. 537–539, 2010.
- [10] B. Fournier, M. Sauzay, and A. Pineau, "Micromechanical model of the high temperature cyclic behavior of 9–12%Cr martensitic steels," *International Journal of Plasticity*, vol. 27, no. 11, pp. 1803–1816, 2011.
- [11] D. C. Madeleine, *Microstructure of Steels and Cast Iron*, Springer, Paris, France, 2003.
- [12] R. Idczak, R. Konieczny, and J. Chojcan, "An enthalpy of solution of chromium in iron studied with ^{57}Fe Mössbauer spectroscopy," *Physica B*, vol. 407, no. 12, pp. 2078–2081, 2012.
- [13] I. Claussen, R. A. Brand, H. Hahn, and S. G. Mayr, "Relaxation scenarios in Fe–Pd and Fe–Pd–Cu ferromagnetic shape memory splats: short range order and microstructure," *Scripta Materialia*, vol. 66, no. 3-4, pp. 163–166, 2012.
- [14] D. M. Minic, D. M. Minic, T. Zak, P. Roupčova, and B. David, "Structural transformations of $\text{Fe}_{81}\text{B}_{13}\text{Si}_4\text{C}_2$ amorphous alloy induced by heating," *Journal of Magnetism and Magnetic Materials*, vol. 323, no. 5, pp. 400–404, 2011.
- [15] F. L. G. Oliveria, M. S. Andrade, and A. B. Cota, "Kinetics of austenite formation during continuous heating in a low carbon steel," *Materials Characterization*, vol. 58, no. 3, pp. 256–261, 2007.
- [16] A. Saha, D. K. Mondal, K. Biswas, and J. Maity, "Microstructural modifications and changes in mechanical properties during cyclic heat treatment of 0.16% carbon steel," *Materials Science and Engineering A*, vol. 534, pp. 465–475, 2012.
- [17] S. A. Sajjadi and S. M. Zebarjad, "Isothermal transformation of austenite to bainite in high carbon steels," *Journal of Materials Processing Technology*, vol. 189, no. 1–3, pp. 107–113, 2007.
- [18] G. Thewlis, "Classification and quantification of microstructures in steels," *Materials Science and Technology*, vol. 20, no. 2, pp. 143–160, 2004.
- [19] E. Güler, "Phase transitions in a high-chromium and medium-carbon steel," *Materials Chemistry and Physics*, vol. 107, no. 2-3, pp. 183–185, 2008.

Research Article

Tuning of Transport and Magnetic Properties in Epitaxial $\text{LaMnO}_{3+\delta}$ Thin Films

J. Chen,¹ L. Hu,¹ W. J. Lu,¹ B. Yuan,¹ K. J. Zhang,¹ J. M. Dai,¹ and Y. P. Sun^{1,2,3}

¹ Key Laboratory of Materials Physics, Institute of Solid State Physics, Chinese Academy of Sciences, Hefei 230031, China

² High Magnetic Field Laboratory, Chinese Academy of Sciences, Hefei 230031, China

³ University of Science and Technology of China, Hefei 230026, China

Correspondence should be addressed to L. Hu; huling@issp.ac.cn and W. J. Lu; wjlu@issp.ac.cn

Received 28 December 2013; Accepted 16 January 2014; Published 19 February 2014

Academic Editor: Ran Ang

Copyright © 2014 J. Chen et al. This is an open access article distributed under the Creative Commons Attribution License, which permits unrestricted use, distribution, and reproduction in any medium, provided the original work is properly cited.

The effect of compressive strain on the transport and magnetic properties of epitaxial $\text{LaMnO}_{3+\delta}$ thin films has been investigated. It is found that the transport and magnetic properties of the $\text{LaMnO}_{3+\delta}$ thin films grown on the LaAlO_3 substrates can be tuned by the compressive strain through varying film thickness. And the insulator-metal transition, charge/orbital ordering transition, and paramagnetic-ferromagnetic transition are suppressed by the compressive strain. Consequently, the related electronic and magnetic transition temperatures decrease with an increase in the compressive strain. The present results can be explained by the strain-controlled lattice deformation and the consequent orbital occupation. It indicates that the lattice degree of freedom is crucial for understanding the transport and magnetic properties of the strongly correlated $\text{LaMnO}_{3+\delta}$.

1. Introduction

Perovskite manganese oxides $\text{La}_{1-x}\text{A}_x\text{MnO}_3$ (A = alkaline earth) have attracted a great deal of attention due to their interesting properties such as colossal magnetoresistance (CMR), charge/orbital ordering (COO), and insulator-metal transition (IMT) [1–3]. The interesting properties originate from the strong correlation of charge, orbital, spin, and lattice degrees of freedom. In this family, the substitution of divalent A for La introduces hole carriers in the Mn 3D band and oxidizes Mn^{3+} to Mn^{4+} , which results in the ferromagnetic metal (FMM) state in terms of double exchange (DE) interaction [4]. In particular, even if without chemical substitution, the LaMnO_3 compound also exhibits a wide range of oxygen nonstoichiometry, which involves the oxidation of some Mn^{3+} to Mn^{4+} in samples of global composition $\text{LaMnO}_{3+\delta}$. However, the insertion of excess oxygen is impossible in the perovskite structure as there is no straightforward way of accommodating any extra oxygen in the close-packed structure. The oxygen nonstoichiometry in $\text{LaMnO}_{3+\delta}$ is incorporated via cation vacancies on both A and B sites [5]. Therefore, the actual crystallographic formula of

such compositions should be written as $\text{La}_{1-x}\text{Mn}_{1-x}\text{O}_3$, with $x = \delta/(3 + \delta)$ [6].

The structure, transport, and magnetic properties of $\text{LaMnO}_{3+\delta}$ highly depend on the value of δ [7–9]. As $0 \leq \delta \leq 0.04$, the crystallographic structure of $\text{LaMnO}_{3+\delta}$ is orthorhombic structure (Pbmn, $c/\sqrt{2} < a < b$) and is strongly Jahn-Teller (JT) distorted; with the δ increasing, the structure changes to the slightly JT distorted orthorhombic structure (Pbmn, $a \leq c/\sqrt{2} < b$); when the $\delta > 0.1$, it falls into the rhombohedral structure. Ritter et al. reported that a small fraction of FMM phase appears in $\text{LaMnO}_{3.07}$ due to the local $\text{Mn}^{3+}\text{-O-Mn}^{4+}$ DE interaction [10]. Furthermore, the COO phase emerges at low temperatures below ~ 110 K, which is far below the FM transition temperature (~ 150 K) for the $\delta = 0.07$ and 0.1 samples. The magnetization measurement results of the samples ($0.085 \leq \delta \leq 0.125$) show a step-like jump at T_C and T_{COO} [11]. Meanwhile Choi et al. reported that a giant softening by 30 cm^{-1} of the 490 and 620 cm^{-1} JT and breathing optical phonon modes had been observed by Raman spectroscopy below T_C in the $\text{LaMnO}_{3+\delta}$ ($0.085 \leq \delta \leq 0.125$) compounds [12]. The results indicate the importance of the electron-phonon coupling in the appearance of COO

phase. For these $\text{LaMnO}_{3+\delta}$ ($0.085 \leq \delta \leq 0.125$) compounds, with decreasing temperature these samples exhibit transition from a paramagnetic insulator (PMI) to FMM at T_C , where the resistivity starts to decrease. At low temperatures, the samples undergo transition from FMM state to COO state at T_{COO} , while the resistivity shows an upturn. This COO phase coexists with the isotropic three-dimensional FM state in spite of the insulating behavior. The overall behaviors of $\text{LaMnO}_{3+\delta}$ ($0.085 \leq \delta \leq 0.125$) compounds are quite similar to those of the lightly doped $\text{La}_{1-x}\text{Sr}_x\text{MnO}_3$ ($0.11 < x < 0.15$) [13, 14].

The study on the lightly doped $\text{La}_{1-x}\text{Sr}_x\text{MnO}_3$, the counterpart of the $\text{LaMnO}_{3+\delta}$, has verified the essential role of lattice deformation in the formation of COO phase. Chen et al. succeeded in realizing the COO phase in the $\text{La}_{7/8}\text{Sr}_{1/8}\text{MnO}_3$ thin films induced by the anisotropic strains on (011) SrTiO_3 substrates [15]. Wang et al. uncovered that the in-plane tensile strain in the $\text{La}_{7/8}\text{Sr}_{1/8}\text{MnO}_3$ thin film grown on the $0.7\text{Pb}(\text{Mg}_{1/3}\text{Nb}_{2/3})\text{O}_3-0.3\text{PbTiO}_3$ substrate can induce COO [16]. However, few works have been reported on the strain effect on the properties of nonstoichiometric $\text{LaMnO}_{3+\delta}$ thin films. Zheng et al. found that the JT distortion of MnO_6 reduces the charge coupling of the $\text{LaMnO}_{3+\delta}$ thin film under an in-plane tensile strain on $0.7\text{Pb}(\text{Mg}_{1/3}\text{Nb}_{2/3})\text{O}_3-0.3\text{PbTiO}_3$ substrate [17, 18]. In this letter, the epitaxial $\text{LaMnO}_{3+\delta}$ thin films have been fabricated on (001)-oriented LaAlO_3 substrate, and in-plane compressive strains have been modified by varying the thickness of thin film. The effect of compressive strain on COO transition and FM transition of the films has been systematically investigated.

2. Experimental

The $\text{LaMnO}_{3+\delta}$ thin films were grown on single crystal substrates by dc magnetron sputtering. We chose (001)-oriented LaAlO_3 (LAO) and (001)-oriented SrTiO_3 (STO) as substrates, and the lattice parameters of the substrates are $a_{\text{LAO}} = 3.792 \text{ \AA}$ and $a_{\text{STO}} = 3.905 \text{ \AA}$. The deposition temperature is 700°C and there are 10 Pa oxygen-argon mixed gases flowing during deposition. After deposition, the films were *in situ* cooled to room temperature in the deposition atmosphere. The thickness of the films was controlled by the deposition time. The degree of orientation and crystallographic characterization of the $\text{LaMnO}_{3+\delta}$ thin films were measured on X-Pert-PRO system using $\text{Cu K}\alpha$ radiation. The superconducting quantum interference device (SQUID) magnetometer was used to measure the magnetic properties of the $\text{LaMnO}_{3+\delta}$ thin films and electrical properties were performed by four-electrode method in a physical property measurement (PPMS) system.

3. Results and Discussion

Figure 1(a) shows the XRD $\theta-2\theta$ scan for the $\text{LaMnO}_{3+\delta}/\text{LAO}$ thin film of thickness $\sim 50 \text{ nm}$. The $\text{LaMnO}_{3+\delta}$ thin films are c -axis oriented and there are no secondary phases. The inset shows the XRD ϕ scans on the $\text{LaMnO}_{3+\delta}$ (101) and LAO (101) reflections. Fourfold symmetry is clearly seen

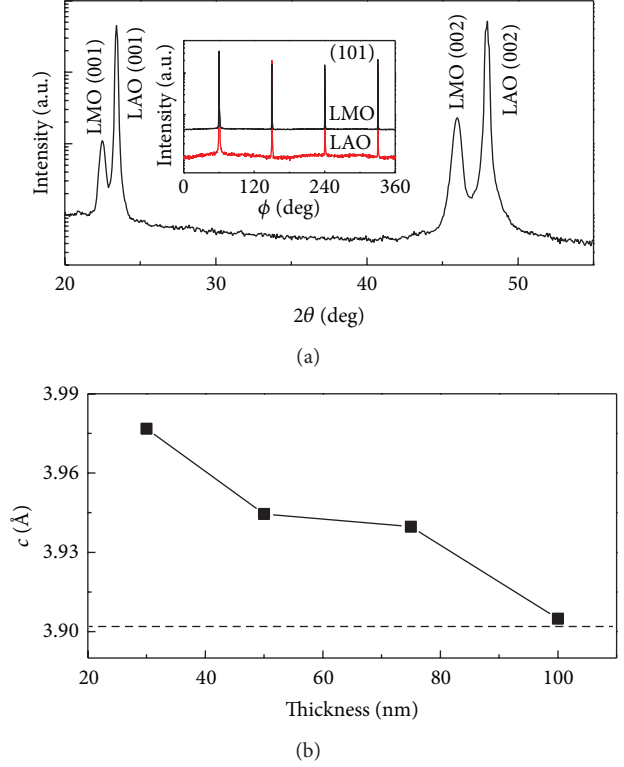


FIGURE 1: (a) XRD pattern of the 50 nm $\text{LaMnO}_{3+\delta}/\text{LAO}$. The inset shows the XRD ϕ scans on the LAO (101) and $\text{LaMnO}_{3+\delta}$ (101) reflections, respectively. (b) Film thickness dependence of out-of-plane lattice parameter. The dashed line represents the c values of bulk $\text{LaMnO}_{3+\delta}$.

for both $\text{LaMnO}_{3+\delta}$ thin film and LAO substrate, which is an indication of cubic-on-cubic epitaxial growth of the $\text{LaMnO}_{3+\delta}$ thin films on the LAO substrates. The out-of-plane lattice parameter c of 50 nm $\text{LaMnO}_{3+\delta}/\text{LAO}$ was calculated to be 3.9445 \AA . As mentioned above, the lattice constants of the $\text{LaMnO}_{3+\delta}$ bulk materials vary with δ . By comparing the T_C and T_{COO} of the $\text{LaMnO}_{3+\delta}$ thin films with those of $\text{LaMnO}_{3+\delta}$ bulk materials, it is estimated that the δ of the $\text{LaMnO}_{3+\delta}$ thin films is ~ 0.09 . For $\delta \sim 0.09$, the lattice constant of the $\text{LaMnO}_{3+\delta}$ bulk materials is $\sim 3.903 \text{ \AA}$ [10, 12]. This value is smaller than that of the 50 nm $\text{LaMnO}_{3+\delta}/\text{LAO}$, indicating that the films are subjected to in-plane compressive and out-of-plane tensile strain. Figure 1(b) shows the out-of-plane lattice parameters of the $\text{LaMnO}_{3+\delta}/\text{LAO}$ depending on the film thickness. Clearly, for the 30 nm $\text{LaMnO}_{3+\delta}/\text{LAO}$ thin film, the out-of-plane lattice parameter is larger than that of the bulk material, which indicates that there exists in-plane compressive strain in the $\text{LaMnO}_{3+\delta}/\text{LAO}$ thin film. With the increasing of film thickness, the out-of-plane lattice parameter decreases and approaches the value of the bulk material. The results show that the in-plane compressive strain of the $\text{LaMnO}_{3+\delta}/\text{LAO}$ exhibits a relaxation with the increase of film thickness.

Figure 2(a) shows the temperature-dependent resistivity of the $\text{LaMnO}_{3+\delta}/\text{LAO}$. The $\text{LaMnO}_{3+\delta}/\text{LAO}$ presents a large variation of electrical transport properties with the

increase of film thickness. For the 30 nm $\text{LaMnO}_{3+\delta}/\text{LAO}$, it exhibits insulating behavior in the whole temperature range. For the 50 nm, 75 nm, and 100 nm $\text{LaMnO}_{3+\delta}/\text{LAO}$, with lowering temperature these films exhibit IMT at T_{IMT} , where the resistivity starts to decrease. The FMM state undergoes a transition to COO state at T_{COO} , while the resistivity shows an upturn. The $T_{\text{IMT}}(T_{\text{COO}})$ of the 50 nm, 75 nm, and 100 nm $\text{LaMnO}_{3+\delta}/\text{LAO}$ are 182 (94) K, 186 (139) K, and 194 (141) K, respectively. Furthermore, both transition temperatures T_{IMT} and T_{COO} of the $\text{LaMnO}_{3+\delta}/\text{LAO}$ can be enhanced by an external magnetic field. As shown by the dashed line in Figure 2(a), the magnetic field of 5 T increases the T_{IMT} and T_{COO} of 50 nm $\text{LaMnO}_{3+\delta}/\text{LAO}$ to 208 K and 110 K, respectively. The results indicate that the magnetic field could stabilize the COO phase in $\text{LaMnO}_{3+\delta}$ thin films, which is similar to the reported in the lightly doped $\text{La}_{1-x}\text{Sr}_x\text{MnO}_3$ ($0.11 < x < 0.15$) [19]. Figure 2(b) presents the temperature dependence of resistivity of the $\text{LaMnO}_{3+\delta}/\text{STO}$ thin film. The electrical transport properties of $\text{LaMnO}_{3+\delta}/\text{STO}$ are almost independent of the film thickness, in contrast to those of $\text{LaMnO}_{3+\delta}/\text{LAO}$. The 30 and 100 nm $\text{LaMnO}_{3+\delta}/\text{STO}$ exhibit two successive transitions upon cooling: high-temperature PMI phase to intermediate FMM phase and then to low-temperature COO phase at T_{COO} . The $T_{\text{IMT}}(T_{\text{COO}})$ of the 30 nm and 100 nm $\text{LaMnO}_{3+\delta}/\text{LAO}$ are 125 (206) K and 134 (205) K, respectively.

Figure 3 shows the temperature dependence of the field-cooled (FC) magnetization under a field of 0.1 T for the $\text{LaMnO}_{3+\delta}/\text{LAO}$. The FM transition temperature T_C is defined as the inflection point in the $M-T$ curves. Similar to the transport properties, the magnetic properties of $\text{LaMnO}_{3+\delta}/\text{LAO}$ are strongly dependent on the film thickness as well. The 30, 50, 75, and 100 nm $\text{LaMnO}_{3+\delta}/\text{LAO}$ exhibit the T_C of 203, 205, 210, and 220 K. The T_C values of the $\text{LaMnO}_{3+\delta}/\text{LAO}$ increase with the increase of the film thickness.

The variation of the transport and magnetic properties of the $\text{LaMnO}_{3+\delta}/\text{LAO}$ with the film thickness suggests the essential role of the lattice degree of freedom. In $\text{LaMnO}_{3+\delta}/\text{LAO}$ under large compressive strain, the MnO_6 octahedra are stretched at the out-of-plane direction and compressed in the in-plane. The lattice distortion can make electrons tend to occupy the $d_{3z^2-r^2}$ orbital and the in-plane transfer integral for the FM-DE decreases, leading to a lower T_C and the insulating transport behavior [20]. With the decrease of the compressive strain, the $d_{3z^2-r^2}$ orbital occupation is weakened and the T_C is increased with the film thickness. Another important feature is the evolution of the COO transition of $\text{LaMnO}_{3+\delta}/\text{LAO}$ with the compressive strain. For the 30 nm $\text{LaMnO}_{3+\delta}/\text{LAO}$, the COO transition is quenched and the film exhibits insulating behavior in the whole temperature range. Furthermore, the T_{COO} increases with the decrease (increase) of in-plane compressive strain (film thickness). It is well known that the occurrence of COO transition in bulk material of $\text{LaMnO}_{3+\delta}$ is intimately correlated with structural anomalies that c -axis increases and a -, b -axes decrease [10]. The lattice deformation associated with the structural anomalies would prefer an occupation of special orbital arrangements that are characteristic of COO

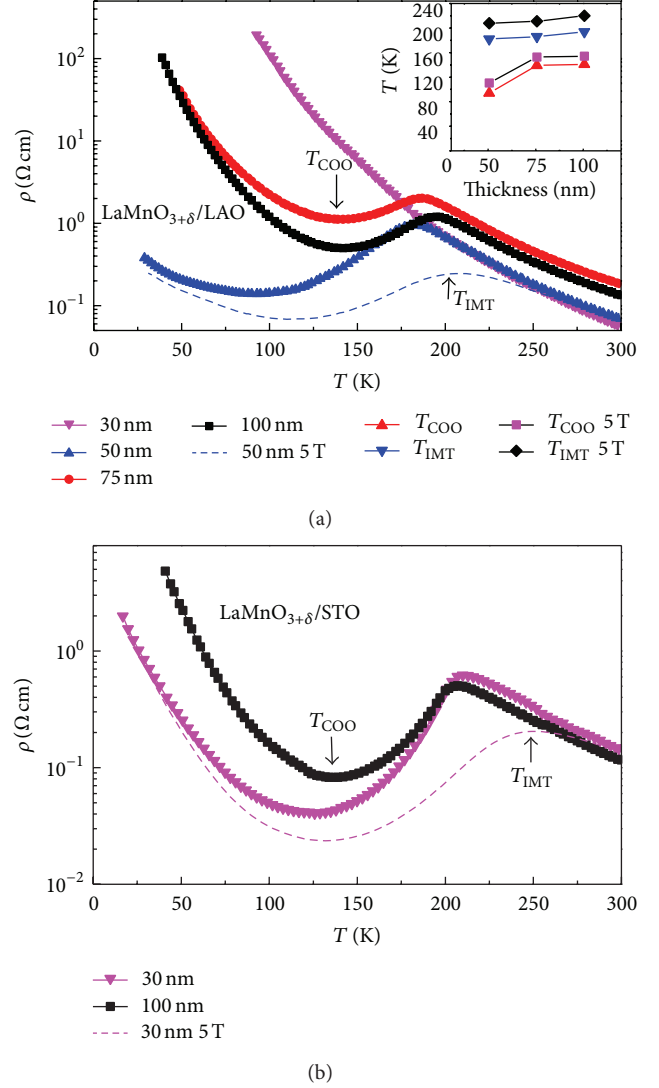


FIGURE 2: Temperature dependence of resistivity for (a) $\text{LaMnO}_{3+\delta}/\text{LAO}$ and (b) $\text{LaMnO}_{3+\delta}/\text{STO}$ film. In (a) solid lines with symbol are zero field results and dashed lines are results of the 50 nm $\text{LaMnO}_{3+\delta}/\text{LAO}$ thin film under 5 T applied field; the inset shows the thickness dependence of the T_{COO} (T_{IMT}) at zero field and the T_{COO} (T_{IMT}) at 5 T field. In (b) solid lines with symbol are zero field results and dashed lines are results of the 30 nm $\text{LaMnO}_{3+\delta}/\text{LAO}$ thin film with 5 T applied field.

[19, 21, 22]. For the $\text{LaMnO}_{3+\delta}$ thin films, the epitaxial strain provided by the substrate would clamp the in-plane lattice of the film. As a result, the lattice deformation associated with structural anomalies of $\text{LaMnO}_{3+\delta}$ thin films would be largely diminished by the epitaxial strain. For the thinnest 30 nm $\text{LaMnO}_{3+\delta}/\text{LAO}$, the in-plane lattice constants are fixed to that of LAO substrate and the out-of-plane lattice parameter is elongated due to the large compressive strain. Consequently, no COO transition is observed. As shown in Figure 1(b), the compressive strain and the clamp effect decrease with the increase of the film thickness. Then the presence of COO phase at low temperatures is expected to

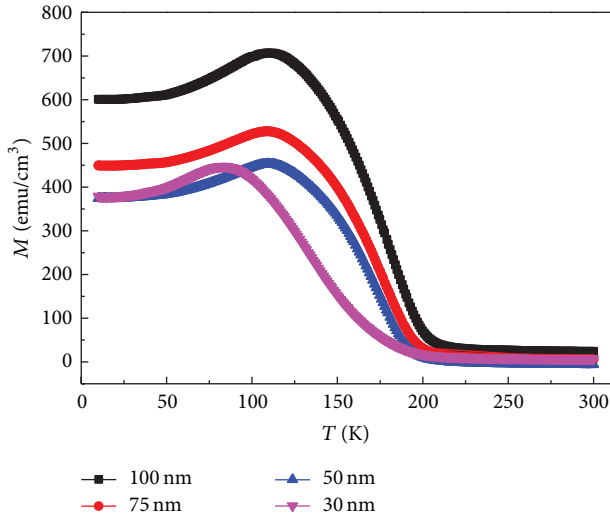


FIGURE 3: FC temperature-dependent magnetization under a field of 0.1 T for $\text{LaMnO}_{3+\delta}/\text{LAO}$.

appear in thicker films and T_{COO} increases with the increase of film thickness. For the $\text{LaMnO}_{3+\delta}/\text{STO}$ with negligible compressive strain, the suppression of lattice deformation and the associated structural anomalies by the STO substrate can be neglected. Consequently, the $\text{LaMnO}_{3+\delta}/\text{STO}$ films with different thickness show bulk-like behavior and the COO transitions are independent of the film thickness, as shown in Figure 2(b). These results verify that the transport and magnetic properties of the $\text{LaMnO}_{3+\delta}$ thin film can be tuned by the epitaxial compressive strain and confirm the importance of the lattice degree of freedom in the $\text{LaMnO}_{3+\delta}$ compound.

4. Conclusion

In summary, the effect of compressive strain induced by substrate on the transport and magnetic properties of $\text{LaMnO}_{3+\delta}$ thin films has been investigated. It was found that the transport and magnetic properties of $\text{LaMnO}_{3+\delta}$ thin films could be tuned by the compressive strain. We demonstrated that the T_{IMT} , T_{COO} , and T_{C} increase with the decrease of the compressive strain. These results indicate the vital role of lattice degree of freedom and the importance of coupling among charge, orbital, spin, and lattice in $\text{LaMnO}_{3+\delta}$.

Conflict of Interests

The authors declare that there is no conflict of interests regarding the publication of this paper.

Acknowledgments

This work was supported by the National Nature Science Foundation of China under Contract nos. 11274311, 10904147, and 11104273, the Joint Funds of the National Natural Science Foundation of China and the Chinese Academy of Sciences'

Large-scale Scientific Facility (Grand no. U1232210), and the Knowledge Innovation Program of the Chinese Academy of Sciences under Contract no. Y04N371121.

References

- [1] J. M. D. Coey, M. Viret, and S. von Molnár, "Mixed-valence manganites," *Advances in Physics*, vol. 48, no. 2, pp. 167–293, 1999.
- [2] Y. Tokura, "Critical features of colossal magnetoresistive manganites," *Reports on Progress in Physics*, vol. 69, no. 3, pp. 797–851, 2006.
- [3] M. B. Salamon and M. Jaime, "The physics of manganites: structure and transport," *Reviews of Modern Physics*, vol. 73, no. 3, pp. 583–628, 2001.
- [4] T. N. Tarasenko, A. S. Mazur, O. F. Demidenko et al., "Crystal structure and lattice defects of $\text{La}_x\text{MnO}_{3+\delta}$," *Inorganic Materials*, vol. 48, no. 10, pp. 1039–1043, 2012.
- [5] R. Mahendiran, S. K. Tiwary, A. K. Raychaudhuri et al., "Structure, electron-transport properties, and giant magnetoresistance of hole-doped LaMnO_3 systems," *Physical Review B*, vol. 53, no. 6, pp. 3348–3358, 1996.
- [6] G. Subías, J. García, J. Blasco, and M. G. Proietti, "Effect of cation vacancies in the local structure and transport properties of $\text{LaMnO}_{3+\delta}$: a Mn K-edge x-ray-absorption study," *Physical Review B*, vol. 58, no. 14, pp. 9287–9293, 1998.
- [7] Q. Huang, A. Santoro, J. W. Lynn et al., "Structure and magnetic order in undoped lanthanum manganite," *Physical Review B*, vol. 55, no. 22, pp. 14987–14999, 1997.
- [8] J. Töpfer and J. B. Goodenough, " $\text{LaMnO}_{3+\delta}$ revisited," *Journal of Solid State Chemistry*, vol. 130, no. 1, pp. 117–128, 1997.
- [9] F. Prado, R. D. Sánchez, A. Caneiro, M. T. Causa, and M. Tovar, "Discontinuous evolution of the highly distorted orthorhombic structure and the magnetic order in $\text{LaMnO}_{3\pm\delta}$ perovskite," *Journal of Solid State Chemistry*, vol. 146, no. 2, pp. 418–427, 1999.
- [10] C. Ritter, M. R. Ibarra, J. M. de Teresa et al., "Influence of oxygen content on the structural, magnetotransport, and magnetic properties of $\text{LaMnO}_{3+\delta}$," *Physical Review B*, vol. 56, no. 14, pp. 8902–8911, 1997.
- [11] S. N. Barilo, V. I. Gatařskaya, S. V. Shiryayev et al., "A study of magnetic ordering in $\text{LaMnO}_{3+\delta}$ single crystals," *Physics of the Solid State*, vol. 45, no. 1, pp. 146–153, 2003.
- [12] K.-Y. Choi, Y. G. Pashkevich, V. P. Gnezdilov et al., "Orbital fluctuating state in ferromagnetic insulating $\text{LaMnO}_{3+\delta}$ ($0.085 \leq \delta \leq 0.125$) studied using Raman spectroscopy," *Physical Review B*, vol. 74, no. 6, Article ID 064406, 2006.
- [13] B. Dabrowski, X. Xiong, Z. Bukowski et al., "Structure-properties phase diagram for $\text{La}_{1-x}\text{Sr}_x\text{MnO}_3$ ($0.1 \leq x \leq 0.2$)," *Physical Review B*, vol. 60, no. 10, pp. 7006–7017, 1999.
- [14] J. Geck, P. Wochner, D. Bruns et al., "Rearrangement of the orbital-ordered state at the metal-insulator transition of $\text{La}_{7/8}\text{Sr}_{1/8}\text{MnO}_3$," *Physical Review B*, vol. 69, no. 10, Article ID 104413, 9 pages, 2004.
- [15] Y. Z. Chen, J. R. Sun, A. D. Wei, W. M. Lu, S. Liang, and B. G. Shen, "Charge ordering transition near the interface of the (011)-oriented $\text{La}_{1-x}\text{Sr}_x\text{MnO}_3$ ($x \sim 1/8$) films," *Applied Physics Letters*, vol. 93, no. 15, Article ID 152515, 2008.
- [16] J. Wang, F. X. Hu, R. W. Li, J. R. Sun, and B. G. Shen, "Strong tensile strain induced charge/orbital ordering in (001)- $\text{La}_{7/8}\text{Sr}_{1/8}\text{MnO}_3$ thin film on $0.7\text{Pb}(\text{Mg}_{1/3}\text{Nb}_{2/3})\text{O}_3-0.3$

- PbTiO₃,” *Applied Physics Letters*, vol. 96, no. 5, Article ID 052501, 2010.
- [17] R. K. Zheng, H.-U. Habermeier, H. L. W. Chan, C. L. Choy, and H. S. Luo, “Effects of substrate-induced strain on transport properties of LaMnO_{3+δ} and CaMnO₃ thin films using ferroelectric poling and converse piezoelectric effect,” *Physical Review B*, vol. 81, no. 10, Article ID 104427, 2010.
- [18] R. K. Zheng, Y. Wang, H. L. W. Chan, C. L. Choy, and H. S. Luo, “Control of the strain and magnetoresistance of LaMnO_{3+δ} thin films using the magnetostriction of Terfenol-D alloy,” *Journal of Applied Physics*, vol. 108, no. 12, Article ID 124103, 2010.
- [19] S. Uhlenbruck, R. Teipen, R. Klingeler et al., “Interplay between charge order, magnetism, and structure in La_{0.875}Sr_{0.125}MnO₃,” *Physical Review Letters*, vol. 82, no. 1, pp. 185–188, 1999.
- [20] A. Sadoc, B. Mercey, C. Simon, D. Grebille, W. Prellier, and M. Lepetit, “Large increase of the Curie temperature by orbital ordering control,” *Physical Review Letters*, vol. 104, no. 4, Article ID 046804, 2010.
- [21] H. Kawano, R. Kajimoto, M. Kubota, and H. Yoshizawa, “Ferromagnetism-induced reentrant structural transition and phase diagram of the lightly doped insulator La_{1-x}Sr_xMnO₃ ($x \leq 0.17$),” *Physical Review B*, vol. 53, no. 22, pp. R14709–R14712, 1996.
- [22] Y. Endoh, K. Hirota, S. Ishihara et al., “Transition between two ferromagnetic states driven by orbital ordering in La_{0.88}Sr_{0.12}MnO₃,” *Physical Review Letters*, vol. 82, no. 21, pp. 4328–4331, 1999.

Research Article

Defects Induced Room Temperature Ferromagnetism in ZnO Thin Films

Xiao Zhang, Wei Zhang, Xinghua Zhang, Xuewen Xu, Fanbin Meng, and C. C. Tang

School of Materials Science and Engineering, Hebei University of Technology, Tianjin 300130, China

Correspondence should be addressed to Xiao Zhang; zhangxiaonk@gmail.com and C. C. Tang; tangcc@hebut.edu.cn

Received 2 December 2013; Accepted 27 December 2013; Published 19 February 2014

Academic Editor: Shoubao Zhang

Copyright © 2014 Xiao Zhang et al. This is an open access article distributed under the Creative Commons Attribution License, which permits unrestricted use, distribution, and reproduction in any medium, provided the original work is properly cited.

Polycrystalline ZnO thin films are prepared by the co-sputtering method under different oxygen partial pressures. Films deposited in pure argon gas exhibit ferromagnetism, whereas other films deposited under different oxygen partial pressures are diamagnetism. XPS results show the presence of Zn interstitial and oxygen vacancy in all of samples. Further analysis indicates that Zn interstitial may play an important role in triggering magnetic order on the undoped ZnO thin films by inducing an alteration of electronic configuration.

1. Introduction

ZnO-based dilute magnetic semiconductors (DMSs) have attracted intense interests due to their potential applications in spintronic devices [1]. Room temperature (RT) ferromagnetism (FM) has been reported theoretically and experimentally in magnetic transition metal doped ZnO nanoparticles and thin films [2–7]. However, several works pointed out that the transition metal dopants are not essential in the observed ferromagnetism. For instance, the results of X-ray magnetic circular dichroism spectra showed that the magnetism in Mn doped ZnO nanoparticle and thin films is critically sensitive to defects other than the transition metal dopants themselves [8] and bulk ZnO doped with Co, Mn, or Cr shows paramagnetism [6, 9, 10]. Meanwhile, RT FM was observed in nonmagnetic ion doped ZnO thin films and nanoparticles [11–13] and even undoped ZnO films [14–17], nanoparticles [18, 19], or partially oxidized Zn nanowires [20, 21], which indicates that the RT FM observed in ZnO matrix may be intrinsic. It is restricted to some defect-rich regions, such as the surface, interface, and grain boundary, not uniform throughout the samples [22]. On the other hand, the indirect exchange interaction models such as Zener/Ruderman-Kittel-Kasuya-Yosida (RKKY)-type exchange, double- and super-exchange, F-center-mediated bound magnetic polaron models, are hard to explain the observed RT FM induced

by only few percent of magnetic ions. Thus, the intrinsic defects should be important on the FM order in ZnO-based DMSs. However, which kinds of defects play an important role, how the defects facilitate the magnetic coupling, and how to control these defects are still under intensive debate. Some reports demonstrated that RT FM could stem from the lattice defects such as oxygen vacancy (V_O) or Zn interstitial (Zn_i) in pure ZnO thin films, nanoparticles, and nanowires [17, 23–26]. Straumal et al. [27] demonstrated that FM only appears if the ratio of grain-boundary area to grain volume exceeds a certain threshold value. Sanchez et al. [28] predicted that varying the hydrogen density on the ZnO (0001) surface can achieve reversible switch of surface FM. More interestingly, even absorbing certain organic molecules can induce ferromagnetic-like behavior in undoped ZnO nanoparticles [29]. These results challenge the understanding of the origin and mechanism of FM.

So far, although lots of works have been carried out to explore the origin of RT FM in undoped ZnO, the results are far from convincing and even some of the results are inconsistent, partly because ZnO is a semiconducting material with many species of native defects with quite a few of them behaving as shallow donors. Now, it is known that the native defects depend strongly on preparation methods and conditions. ZnO materials prepared by various methods from different

groups generally show significant differences in physical properties including native defect/impurity species and density, mobility, and crystallinity. When these ZnO materials are employed for DMSs study, it is not a surprise that distinct results were reported even with similar conditions. Therefore, it is the most important to elucidate the effect of specific film-growth conditions. In this study, polycrystalline ZnO films were fabricated under different oxygen partial pressure (P_{O_2}). The experimental results show that the only RT FM observed in ZnO film deposited under pure Ar and saturated magnetization is 0.89 emu/cc, while other samples deposited under Ar and O_2 mixture are diamagnetism. After depositing a single Zn layer on the magnetic film and annealing the sample at high temperature, the saturated magnetization significantly increased to 1.62 emu/cc. These results suggest that the Zn interstitial may be a response to the origin of FM order in pure ZnO thin films.

2. Experiments

A series of polycrystalline ZnO films were fabricated by RF-sputtering ZnO (99.99%) targets in Ar (99.999%) and O_2 (99.999%) mixture at room temperature. The base pressure of the chamber was better than 1×10^{-5} Pa before deposition and the total pressure for sputtering was kept at 2.0 Pa. The RF-sputtering power of ZnO target was kept at 260 W. The films were deposited on glass and kapton substrates for the measurements of structural and transport properties, respectively. To eliminate the spurious magnetic data, the samples and polymer tweezers were cleaned with acetone prior to measurement. The films thickness was kept at 200 nm. The microstructure of the films was characterized by X-ray diffraction pattern (XRD) with Cu K_α radiation ($\lambda = 0.15418$) using X' Pert PRO machine. The composition and chemical states of ZnO thin films were examined by X-ray photoelectron spectroscopy (XPS) and auger electron spectroscopy (AES) using Physical Electronic Spectrometry machine. The DC electrical resistivity measurements were measured using a conventional four-probe method performed in a Quantum Design PPMS. The magnetization measurements were carried out using a Quantum Design vibrating sample magnetometry.

3. Results and Discussion

Figure 1(a) shows the XRD pattern of the ZnO polycrystalline samples fabricated under different oxygen partial pressure (P_{O_2}). The results indicate that all samples have highly (001)-preferred orientation in contrast to the standard diffraction pattern of wurtzite ZnO. The particle size can be derived from the Scherrer formula [30]:

$$D_{hkl} = \frac{0.9\lambda}{\beta \cos \theta}, \quad (1)$$

where D_{hkl} is the particle size along (hkl) direction, β is the full width at half maximum (FWHM) of the XRD peak, $\lambda = 0.154058$ nm is the wavelength of Cu K_α radiation, and θ is the Bragg angle. Figure 1(b) shows the relation between

obtained particle size using the FWHM of (002) peaks and P_{O_2} . It can be seen that there is not monotonic dependence of particle size on the P_{O_2} . At low P_{O_2} , the particle size increases with increasing P_{O_2} , reaches the maximum value at $P_{O_2} = 1$ Pa, and then decreases to 42.7(9) at $P_{O_2} = 1.5$ Pa. With the P_{O_2} increasing, the particle size of the ZnO thin films tends to be a constant.

The composition and chemical states of the ZnO thin films deposited under $P_{O_2} = 0$ Pa and $P_{O_2} = 2$ Pa are further investigated by XPS analysis. Samples were etched by Ar^+ bombardment (5×10^5 Torr) for 5 min to examine the intrinsic chemical state of each element in the films. A broad scan survey spectrum indicates that only Zn, O, and C elements exist and no other detectable contaminated element above 0.1% exists in the ZnO samples. As shown in Figure 2(a) the peak positions of Zn $2p_{1/2}$ and Zn $2p_{3/2}$ are similar in both samples. Comparing the XPS standard spectra of Zn $2p$ [30], it is concluded that the valence state of Zn element is +2. On the other hand, the peaks of Zn $2p_{3/2}$ in both samples exhibit slight asymmetry. Islam group has analyzed the Zn $2p_{3/2}$ peak of ZnO thin film systematically and attributed this kind of asymmetry of Zn $2p_{3/2}$ peak to the existence of excess zinc in the films [31]. No such asymmetry is observed for hydrogen-annealed pure ZnO films. But the exact nature of the distribution of Zn in the ZnO matrix remains under investigation. In order to confirm the existence of zinc in the films, AES measurements were carried out. Figure 2(b) presents a Zn($L_3M_{45}M_{45}$) AES signal of the ZnO samples deposited under $P_{O_2} = 0$ Pa and $P_{O_2} = 2$ Pa. The major peaks at 264.2 eV are considered to be associated with Zn^{2+} in ZnO matrix. The minor one at 261.2 eV is due to Zn of metallic Zn or Zn_i in ZnO matrix lattice. It can be seen that the peak intensity at 261.2 eV for the sample deposited under $P_{O_2} = 0$ Pa is significantly larger than that for sample prepared under $P_{O_2} = 2$ Pa. It implies that more metallic Zn or Zn_i can be generated under oxygen-deficient atmosphere.

Deeper insight into the chemical states of oxygen is achieved through the analysis of the O 1s peaks of ZnO polycrystalline samples deposited under $P_{O_2} = 0$ Pa and $P_{O_2} = 2$ Pa, as shown in Figure 3. The broad and asymmetric O 1s peaks could be consistently fitted by a Gaussian function to separate the multicomponent oxygen species, which centered at 530.0 ± 0.1 eV, 531.5 ± 0.1 eV, and 532.3 ± 0.1 eV, respectively. The component on the low binding energy side of the O 1s at 530.0 ± 0.1 eV is attributed to O^{2-} ions in wurtzite structure of hexagonal Zn^{2+} ion array, surrounded by Zn atoms with their full complement of the nearest neighboring O^{2-} ions [32]. In other words, the intensity of this component is the indicator of the amount of oxygen atoms in a fully oxidized, stoichiometric surrounding. The medium binding energy component at 531.5 ± 0.1 eV may partially be associated with O^{2-} ions that are in oxygen-deficient regions within the matrix. Thus, the variation of the relative intensity ratio of medium component to total O 1s may be connected in part to the variations in the concentration of oxygen vacancies. It can be seen that this ratio for the sample prepared without O_2 is remarkably larger than the sample deposited under $P_{O_2} = 2$ Pa. It is consistent with AES results of Zn; that is,

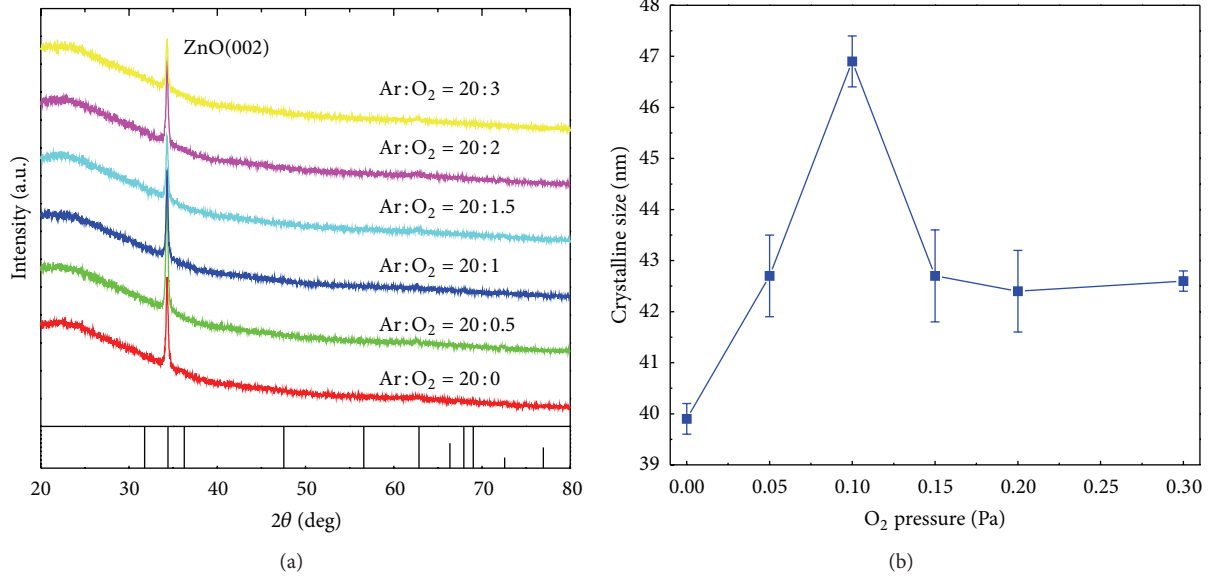


FIGURE 1: (a) XRD patterns of ZnO polycrystalline thin films deposited under different oxygen partial pressure; (b) the average grains diameters as a function of oxygen partial pressure estimated by the Scherrer equation.

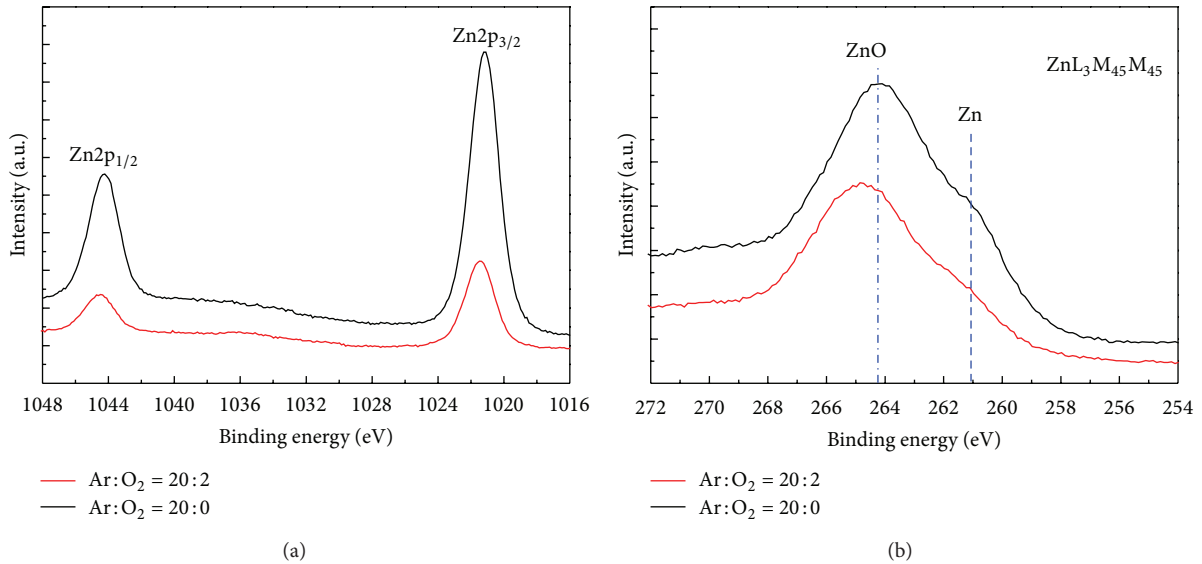


FIGURE 2: (a) XPS data of Zn 2p and (b) AES data of Zn LMM in ZnO films deposited under $P_{O_2} = 0$ Pa and $P_{O_2} = 2$ Pa.

without O₂, more Zn_i and V_O appear when compared to the sample deposited under O₂. Finally, the appearance of the high binding energy component at 532.3 ± 0.1 eV indicates the presence of loosely bound oxygen in the ZnO films belonging to specific species, such as adsorbed H₂O or adsorbed O₂, which is difficult to remove by just increasing P_{O_2} during deposition process.

Figure 4 shows magnetization loops of ZnO films deposited under different P_{O_2} . The applied magnetic field was parallel to the surface of the sample. The data in the main figure is $M-H$ curves before the subtraction of the

diamagnetic signal of samples, which indicates the sample prepared under $P_{O_2} = 0$ Pa shows RT FM. Upper inset of Figure 3 obtained from subtracting the saturated linear parts of the measured signal shows typical hysteresis behaviors and the saturated magnetization is 0.89 emu/cc. However, other samples deposited under different oxygen partial pressure are diamagnetic, confirming that no FM impurities were introduced during the preparation of the films. It should be noted that FM behavior and average grains diameters upon different oxygen partial pressure have different trends. It implies that the average grains sizes are indirectly related

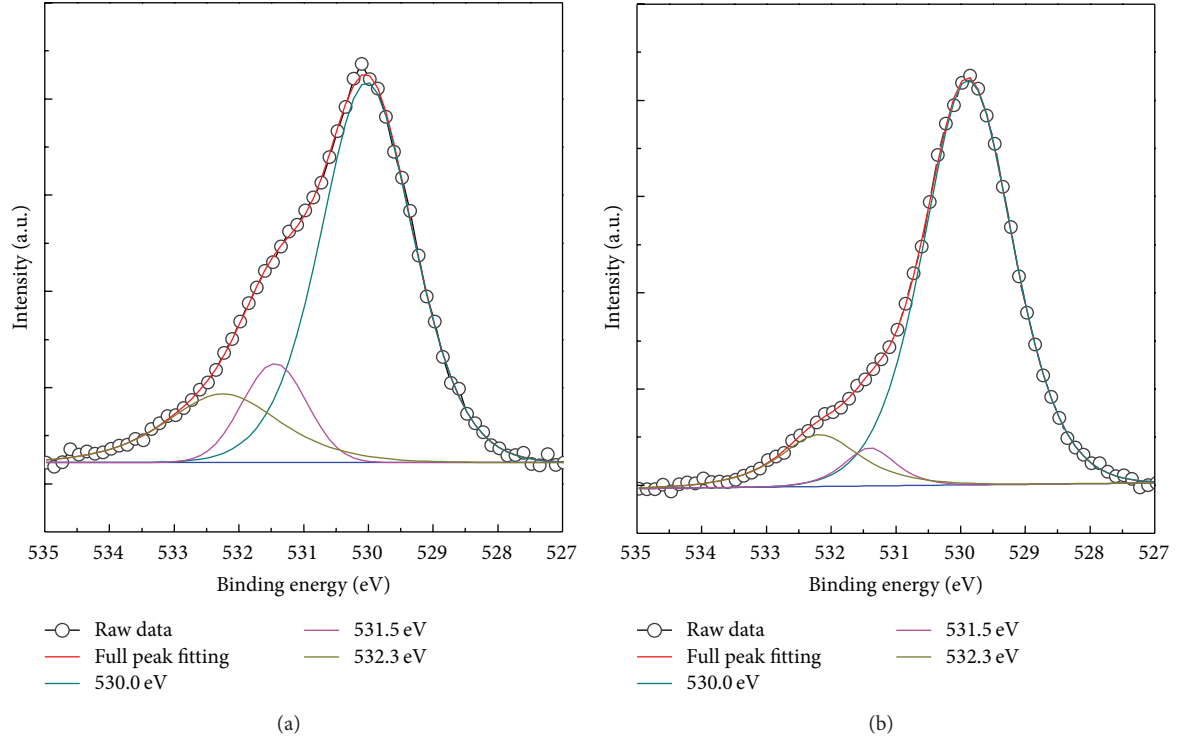


FIGURE 3: XPS data of O 1s and its Gaussian-resolved component for the sample deposited under (a) $P_{O_2} = 0$ Pa and (b) $P_{O_2} = 2$ Pa, respectively.

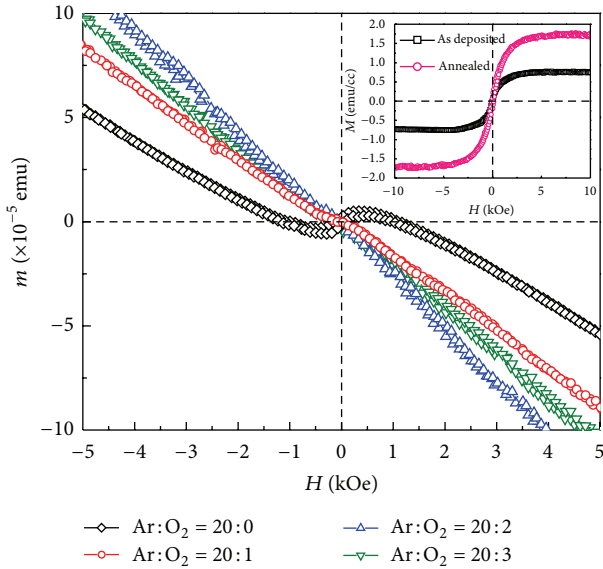


FIGURE 4: M - H curves for ZnO thin films deposited under different oxygen partial pressure at 300 K. Upper inset: M - H curves of ZnO as-deposited and annealed films deposited under $P_{O_2} = 0$ Pa at 300 K after the subtraction of the diamagnetic signal.

to the FM in undoped ZnO films. On the other hand, the measured resistivity of the samples deposited under $P_{O_2} = 0$ Pa is $6.5(2) \times 10^4 \Omega \text{ cm}$ at RT.

Indeed, the origin of RT FM in undoped ZnO is still a controversial issue. Many hypotheses have been presented to give a reasonable interpretation for the origin of the RT FM in pure ZnO. Since the sample deposited under $P_{O_2} = 0$ Pa is insulators, the carrier-mediated RKKY-type model seems not to be applicable. According to previous work [23–26], the origin of the room temperature FM of undoped ZnO is due to the introduction of Zn_i and/or V_O defects rather than Zn vacancies (V_{Zn}), because formation energy of V_{Zn} is so high that it could not preferably form in ZnO. The chemical states of Zn and O ions in ZnO samples deposited under different P_{O_2} show that Zn_i and V_O coexist in the as-deposited samples. As P_{O_2} increases, both of the Zn_i and V_O are decreasing meanwhile the FM disappears at higher P_{O_2} . Thus, the Zn_i and/or V_O should contribute to the origin of FM in pure ZnO thin films. To further confirm which kind of defect plays a more important role in the origin of FM in the sample, a layer of pure Zn with thickness of about 70 nm was deposited on the ZnO film deposited under $P_{O_2} = 0$ Pa. Then, the sample was heated in high vacuum at 300°C for 10 min. Because the diffusion of Zn is easier than that of oxygen [33] and there are not enough oxygen atoms from the air which can diffuse in the lattice to oxidize the diffused Zn, Zn_i will generate and be trapped in the lattice, which leads to the increase in defect density of Zn_i . On the other hand, magnetic measurement indicates that the saturated magnetization of annealed sample increases to 1.62 emu/cc. Thus, Zn_i not V_O should be responsible for the observed weak RT FM in as-deposited sample and the significant increase of M_s in the annealed sample.

Theoretical calculation indicated that the level of Zn_i lies close to the bottom of the conduction band (shallow donors), which will induce strong interaction between the localized interstitial Zn 4s level and the conduction band [5]. This interaction alternates the electronic structure, leading to ferromagnetic-like behavior. It should be noted that this modification of the semiconductor electronic structure can be realized in the absence of the magnetic ions. More generally, other methods inducing such kind of shallow donors will also alternate the electronic structure and result in the RT FM, such as fabricating ZnO low dimensional nanoparticles with more intrinsic defects, capping with organic molecules into ZnO nanoparticle [29] and producing more defects by mechanical milling in ZnO nanoparticles [23].

4. Conclusions

In summary, RT FM is observed in undoped ZnO thin films deposited without oxygen, while other samples deposited under different P_{O_2} are all diamagnetism. After depositing a single Zn layer on the magnetic ZnO thin films and annealing the sample at high temperature, the saturated magnetization significantly increased. All results indicate that the origin of FM order in pure ZnO films should be related to the Zn_i defects. The shallow donor caused by Zn_i defects might modify the electronic structure of undoped ZnO thin films, leading to the RT FM. Our result will help to get further insight into the ferromagnetic origin in undoped ZnO systems.

Conflict of Interests

The authors declare that there is no conflict of interests regarding the publication of this paper.

Acknowledgments

This work was supported by the National Natural Science Foundation of China (Grant nos. 51102075, 51171056, and 51371075) and the Key Project of Science and Technology for Colleges in Hebei Province, China (Grant no. ZD2010120).

References

- [1] S. A. Wolf, D. D. Awschalom, R. A. Buhrman et al., "Spintronics: a spin-based electronics vision for the future," *Science*, vol. 294, no. 5546, pp. 1488–1495, 2001.
- [2] T. Dietl, H. Ohno, F. Matsukura, J. Cibert, and D. Ferrand, "Zener model description of ferromagnetism in zinc-blende magnetic semiconductors," *Science*, vol. 287, no. 5455, pp. 1019–1022, 2000.
- [3] J. M. D. Coey, M. Venkatesan, and C. B. Fitzgerald, "Donor impurity band exchange in dilute ferromagnetic oxides," *Nature Materials*, vol. 4, no. 2, pp. 173–179, 2005.
- [4] H. Gu, W. Zhang, Y. Xu, and M. Yan, "Effect of oxygen deficiency on room temperature ferromagnetism in Co doped ZnO," *Applied Physics Letters*, vol. 100, no. 11, Article ID 202401, 2012.
- [5] C. H. Patterson, "Role of defects in ferromagnetism in $Zn_{1-x}Co_xO$: a hybrid density-functional study," *Physical Review B*, vol. 74, no. 14, Article ID 144432, 2006.
- [6] H. Liu, X. Zhang, L. Li et al., "Role of point defects in room-temperature ferromagnetism of Cr-doped ZnO," *Applied Physics Letters*, vol. 91, no. 7, Article ID 072511, 2007.
- [7] J. M. Baik, T. W. Kang, and J.-L. Lee, "Effects of N_2O plasma treatment on magnetic properties of (Zn, Mn)O nanorods," *Nanotechnology*, vol. 18, no. 9, Article ID 095703, 2007.
- [8] K. R. Kittilstved, W. K. Liu, and D. R. Gamelin, "Electronic structure origins of polarity-dependent high- T_c ferromagnetism in oxide-diluted magnetic semiconductors," *Nature Materials*, vol. 5, no. 4, pp. 291–297, 2006.
- [9] J. Alaria, P. Turek, M. Bernard et al., "No ferromagnetism in Mn doped ZnO semiconductors," *Chemical Physics Letters*, vol. 415, no. 4–6, pp. 337–341, 2005.
- [10] S. Yin, M. X. Xu, L. Yang et al., "Absence of ferromagnetism in bulk polycrystalline $Zn_{0.9}Co_{0.1}O$," *Physical Review B*, vol. 73, no. 22, Article ID 224408, 2006.
- [11] M. Venkatesan, C. B. Fitzgerald, J. G. Lunney, and J. M. D. Coey, "Anisotropic ferromagnetism in substituted zinc oxide," *Physical Review Letters*, vol. 93, no. 17, Article ID 177206, p. 1, 2004.
- [12] H. Pan, J. B. Yi, L. Shen et al., "Room-temperature ferromagnetism in carbon-doped ZnO," *Physical Review Letters*, vol. 99, no. 12, Article ID 127201, 2007.
- [13] C.-F. Yu, T.-J. Lin, S.-J. Sun, and H. Chou, "Origin of ferromagnetism in nitrogen embedded ZnO:N thin films," *Journal of Physics D*, vol. 40, no. 21, pp. 6497–6500, 2007.
- [14] Q. Xu, H. Schmidt, S. Zhou et al., "Room temperature ferromagnetism in ZnO films due to defects," *Applied Physics Letters*, vol. 92, no. 8, Article ID 082508, 2008.
- [15] S. Ghoshal and P. S. Anil Kumar, "Suppression of the magnetic moment upon Co doping in ZnO thin film with an intrinsic magnetic moment," *Journal of Physics Condensed Matter*, vol. 20, no. 19, Article ID 192201, 2008.
- [16] M. Kapilashrami, J. Xu, V. Ström, K. V. Rao, and L. Belova, "Transition from ferromagnetism to diamagnetism in undoped ZnO thin films," *Applied Physics Letters*, vol. 95, no. 3, Article ID 033104, 2009.
- [17] N. H. Hong, J. Sakai, and V. Brizé, "Observation of ferromagnetism at room temperature in ZnO thin films," *Journal of Physics Condensed Matter*, vol. 19, no. 3, Article ID 036219, 2007.
- [18] Z. Yan, Y. Ma, D. Wang et al., "Impact of annealing on morphology and ferromagnetism of ZnO nanorods," *Applied Physics Letters*, vol. 92, no. 8, Article ID 081911, 2008.
- [19] J. B. Yi, H. Pan, J. Y. Lin et al., "Ferromagnetism in ZnO nanowires derived from electro-deposition on AAO template and subsequent oxidation," *Advanced Materials*, vol. 20, no. 6, pp. 1170–1174, 2008.
- [20] L. Y. Li, Y. H. Cheng, X. G. Luo et al., "Room-temperature ferromagnetism and the scaling relation between magnetization and average granule size in nanocrystalline Zn/ZnO core-shell structures prepared by sputtering," *Nanotechnology*, vol. 21, no. 14, Article ID 145705, 2010.
- [21] Z. Yang, "A perspective of recent progress in ZnO diluted magnetic semiconductors," *Applied Physics A*, vol. 112, no. 2, pp. 241–254, 2013.
- [22] J. M. D. Coey, K. Wongsaprom, J. Alaria, and M. Venkatesan, "Charge-transfer ferromagnetism in oxide nanoparticles," *Journal of Physics D*, vol. 41, no. 13, Article ID 134012, 2008.

- [23] T. L. Phan, Y. D. Zhang, D. S. Yang, N. X. Nghia, T. D. Thanh, and S. C. Yu, "Defect-induced ferromagnetism in ZnO nanoparticles prepared by mechanical milling," *Applied Physics Letters*, vol. 102, no. 7, Article ID 072408, 2013.
- [24] S. Banerjee, M. Mandal, N. Gayathri, and M. Sardar, "Enhancement of ferromagnetism upon thermal annealing in pure ZnO," *Applied Physics Letters*, vol. 91, no. 18, Article ID 182501, 2007.
- [25] M. H. F. Sluiter, Y. Kawazoe, P. Sharma et al., "First principles based design and experimental evidence for a ZnO-based ferromagnet at room temperature," *Physical Review Letters*, vol. 94, no. 18, Article ID 187204, 2005.
- [26] X. Zhang, Y. H. Cheng, L. Y. Li et al., "Evidence for high- T_c ferromagnetism in $Zn_x (ZnO)_{1-x}$ granular films mediated by native point defects," *Physical Review B*, vol. 80, no. 17, Article ID 174427, 2009.
- [27] B. B. Straumal, A. A. Mazilkin, S. G. Protasova et al., "Magnetization study of nanograined pure and Mn-doped ZnO films: formation of a ferromagnetic grain-boundary foam," *Physical Review B*, vol. 79, no. 20, Article ID 205206, 2009.
- [28] N. Sanchez, S. Gallego, J. Cerdá, and M. C. Muñoz, "Tuning surface metallicity and ferromagnetism by hydrogen adsorption at the polar ZnO(0001) surface," *Physical Review B*, vol. 81, no. 11, Article ID 115301, 2010.
- [29] M. A. Garcia, J. M. Merino, E. F. Pinel et al., "Magnetic properties of ZnO nanoparticles," *Nano Letters*, vol. 7, no. 6, pp. 1489–1494, 2007.
- [30] B. D. Cullity, *Elements of X-Ray Diffraction*, Addison-Wesley Publication, New York, NY, USA, 1978.
- [31] M. N. Islam, T. B. Ghosh, K. L. Chopra, and H. N. Acharya, "XPS and X-ray diffraction studies of aluminum-doped zinc oxide transparent conducting films," *Thin Solid Films*, vol. 280, no. 1-2, pp. 20–25, 1996.
- [32] J. C. C. Fan and J. B. Goodenough, "X-ray photoemission spectroscopy studies of Sn-doped indium-oxide films," *Journal of Applied Physics*, vol. 48, no. 8, pp. 3524–3531, 1977.
- [33] K. R. Kittilstved, D. A. Schwartz, A. C. Tuan, S. M. Heald, S. A. Chambers, and D. R. Gamelin, "Direct kinetic correlation of carriers and ferromagnetism in Co^{2+} :ZnO," *Physical Review Letters*, vol. 97, no. 3, Article ID 037203, 2006.

Research Article

Aging Effect on Electrical Conductivity of Pure and Al-Doped $\text{YBa}_2\text{Cu}_3\text{O}_{7-\delta}$ Single Crystals with a Given Topology of Planar Defects

Ruslan V. Vovk,¹ Nikolaj R. Vovk,¹ and Oleksandr V. Dobrovolskiy^{1,2}

¹ Physical Department, Kharkiv National University, Kharkiv 61077, Ukraine

² Physikalisches Institut, Goethe-University, 60438 Frankfurt am Main, Germany

Correspondence should be addressed to Oleksandr V. Dobrovolskiy; dobrovolskiy@physik.uni-frankfurt.de

Received 18 August 2013; Accepted 25 September 2013

Academic Editor: Hechang Lei

Copyright © 2013 Ruslan V. Vovk et al. This is an open access article distributed under the Creative Commons Attribution License, which permits unrestricted use, distribution, and reproduction in any medium, provided the original work is properly cited.

The conducting properties in the basal ab plane of pure and Al-doped $\text{YBa}_2\text{Cu}_3\text{O}_{7-\delta}$ single crystals before and after long-time exposure in air atmosphere are investigated. It is shown that prolonged aging leads to an increase of the density of effective scattering centers for the normal carriers. The aluminum doping has been revealed to partially slowdown the degradation of the conducting properties in process of aging. The excess conductivity, $\Delta\sigma(T)$, has been found to obey exponential dependence in the broad temperature range $T_c < T < T^*$. In the pseudogap regime, the mean-field transition temperature T^* and the 3D-2D crossover point in the excess conductivity have been quantified. Near the critical temperature, $\Delta\sigma(T)$ is described well within the Aslamazov-Larkin theoretical model. Herewith, both aluminum doping and prolonged aging have been found to essentially expand the temperature interval of implementation of the pseudogap state, thus narrowing the linear section in the dependence $\rho_{ab}(T)$.

1. Introduction

Despite the fact that almost three decades have passed since the discovery of high-temperature superconductivity (HTSC) [1], the microscopic nature of this phenomenon remains definitively unexplained so far. In accordance with the contemporary views, it is assumed that the key for understanding the nature of HTSC can be in scrutinizing the physical phenomena observed in these compounds in the normal state at temperatures at and above the critical temperature T_c . The transitions to the fluctuation and the pseudogap regimes are exemplary for those phenomena. Whereas thousands of papers are devoted to the treatment of physics of the pseudogap state and the fluctuation conductivity in HTSC compounds (see, e.g., [2–6] for reviews), both the nature of the pseudogap state to appear and its role in the formation of the superconducting state still remain unclear.

Along with this, in the recent years there is a tendency to expand the field of studies regarding the technological use of high-temperature superconductors (HTSCs) [7]. This is

mostly associated with a more intensive use of these compounds in contemporary microelectronics, telecommunication systems, and so forth. In this respect, compounds from the system $\text{YBa}_2\text{Cu}_3\text{O}_{7-\delta}$ (1-2-3) are most promising. This is due to several factors as follows. (i) These superconductors have a high critical temperature T_c , above the boiling point of liquid nitrogen. (ii) One can relatively easy alter their structure and conductive properties by varying the oxygen content [8] and by substituting the constituent elements with respective isoelectronic analogues [9]. It should be noted that, in 1-2-3 compounds, there practically always exist planar defects, such as twin boundaries (TBs) that can significantly extend the range of possible research [10]. At the same time, all the aforementioned characteristics are raising new questions and challenges. For example, the presence of labile oxygen in $\text{YBa}_2\text{Cu}_3\text{O}_{7-\delta}$ often leads to a nonequilibrium state in the system, which can be induced by temperature [8, 9] or by high pressure [10–12]. In general, these effects are observed in nonstoichiometric samples in respect of the oxygen content and are absent in samples with low oxygen

deficiency $\delta \leq 0.15$ [13]. At the same time, in the literature, there are a number of works [14–16] which note the possibility of changing the superconducting and electrotransport properties of 1-2-3 samples in the course of prolonged aging in air atmosphere. Therein, the published data are often contradictory. For instance, a significant improvement of the electrotransport and an increase of the critical current in process of long-term annealing are reported in [17]. At the same time, a pronounced degradation of these properties before long-term exposure in ambient air is noted in [14–16].

Altering the composition of 1-2-3 superconductors is also an important instrument to find empirical ways for improving their critical parameters and for extending their technological applications. It is known that a complete or partial substitution of yttrium with rare earth elements, with the exception of praseodymium (the praseodymium anomaly) which suppresses the superconducting parameters of the compound [18], slightly affects their physical characteristics in the normal and the superconducting state [9, 10, 19]. By contrast, an important role is played by the partial replacement of copper by elements such as gold, silver, and aluminum [20–24]. Gold and silver, in small concentrations of these compounds, improve conductivity and prevent degradation of the superconducting properties in the aging process [20, 21]. The published data regarding the impact of aluminum on the electrotransport properties of the compound $\text{YBa}_2\text{Cu}_3\text{O}_{7-\delta}$ still remain unclear and are in essence contradictory. For example, a slight rise in the resistivity ρ_{ab} in the basal ab plane of $\text{YBa}_2\text{Cu}_{3-y}\text{Al}_y\text{O}_{7-\delta}$ crystals at $y \leq 0.1$ was observed in [22]. At the same time, a twofold increase of ρ_{ab} at the same concentration of aluminum is reported in [23]. The reason for this discrepancy is most likely a nonhomogeneous distribution of aluminum over the crystal volume, as during the crystal growth in alundum crucibles the introduction of aluminum occurs in an uncontrolled way. In particular, the nonhomogeneous distribution of aluminum results in broader transitions into the superconducting state ($\Delta T_c \geq 2$ K) and their stepwise form [22, 23]. There is also substantial variation in the superconducting parameters of the samples. It should be noted that aluminum doping facilitates a severalfold reduction of the period of the twin superstructure [24] and, at high concentrations, the formation of intersecting “tweed”-type twin domains [25]. On the one hand, TBs, which are extended planar defects, promote strengthening of the pinning processes [26], thus extending the range of the use of HTSCs in obtaining high magnetic fields. On the other hand, the presence of TBs often complicates the investigation of the resistive characteristics, due to the difficulty of defining their contribution to the electrical conductivity in HTSCs [24]. Thereby, the influence of aluminum doping on aging of 1-2-3 compounds has remained an open question so far.

Taking the above under consideration, the objective of this study is to investigate, in the different conductivity regimes, the effect of prolonged aging in ambient air on the electrotransport properties of pure and Al-doped $\text{YBa}_2\text{Cu}_3\text{O}_{7-\delta}$ single crystals. The samples have a high critical temperature T_c and contain a system of unidirectional TBs. The measurements are carried out with the transport current

I directed parallel to TBs, that is, when the influence of the TBs on the charge carrier scattering is minimal.

2. Sample Preparation

The $\text{YBa}_2\text{Cu}_3\text{O}_{7-\delta}$ single crystals were grown in a gold crucible by the solution-melting method, under small temperature gradient along the crucible [24]. As source components we used powder compounds of Y_2O_3 , BaCO_3 and Cu. To obtain Al-doped single crystals, 0.2 at.% Al_2O_3 was added. After the growth, all the crystals were annealed at 420°C in air atmosphere in order to obtain the optimal oxygen concentration and a high T_c . In all the samples the axis c was oriented along the smallest dimension. For the resistivity measurements, the following single crystals were selected: crystal K1 ($\text{YBa}_2\text{Cu}_3\text{O}_{7-\delta}$) with dimensions of $2 \times 0.3 \times 0.02$ mm³ and crystal K2 ($\text{YBa}_2\text{Cu}_{3-y}\text{Al}_y\text{O}_{7-\delta}$) with dimensions of $2.3 \times 0.75 \times 0.03$ mm³. Both single crystals contained areas with unidirectional TBs, with dimensions of 0.5×0.5 mm². The geometry was selected in such a way that we could cut out bridges with parallel TBs (see also Figure 1(a)), with a width of 0.2 mm and a distance between the voltage contacts of 0.3 mm. The standard four-contact scheme was used to form electric contacts, whose arrangement is shown in the inset of Figure 1(b). In these, gold connectors (0.05 mm in diameter) were attached to the sample surface with silver paste. To make the electrical contacts easier, both wired samples were thereupon annealed in ambient air for several hours. This method provided a contact transient resistance of less than 1Ω and made it possible to measure the resistivity at transport currents up to 10 mA in the ab plane. The temperature was measured with a copper-constantan thermocouple. The first measurements of the electrical resistivity in the basal ab plane were made immediately after removal of the crystals from the melt and saturating them with oxygen to the optimum value ($\delta \leq 0.1$). After these measurements, the crystals were stored in a glass container until the remeasurements, which have been done 6 years later.

We performed an inspection of the elemental composition in the as-grown crystals using energy-dispersive X-ray spectroscopy (EDX). The EDX parameters were 10 kV/2.4 nA and the probed areas were 2×2 μm^2 . Here the beam energy determines the effective thickness of the layer being analyzed, which is approximately 0.7 μm . The penetration of the electrons into the crystal was calculated by the simulation program Casino available at <http://www.gel.usherbrooke.ca/casino/index.html>. The material composition was calculated taking into account ZAF (atomic number, absorption, and fluorescence) and background corrections. The software we used was EDAX's Genesis Spectrum v. 5.10. The statistical error in the elemental composition is 1%. The EDX spectrum for the pure crystal K1 is shown in Figure 1(b). It shows four peaks corresponding to 7.7 at.% of Y, 16.2 at.% of Ba, 23.1 at.% of Cu, and 53 at.% of O. Other elements have not been detected in the as-grown pure crystal K1.

A photograph of the surface of the Al-doped crystal K2, with a characteristic pattern of TBs, is shown in Figure 1(a). As is known, substitutions of 3-valent ions are centers for

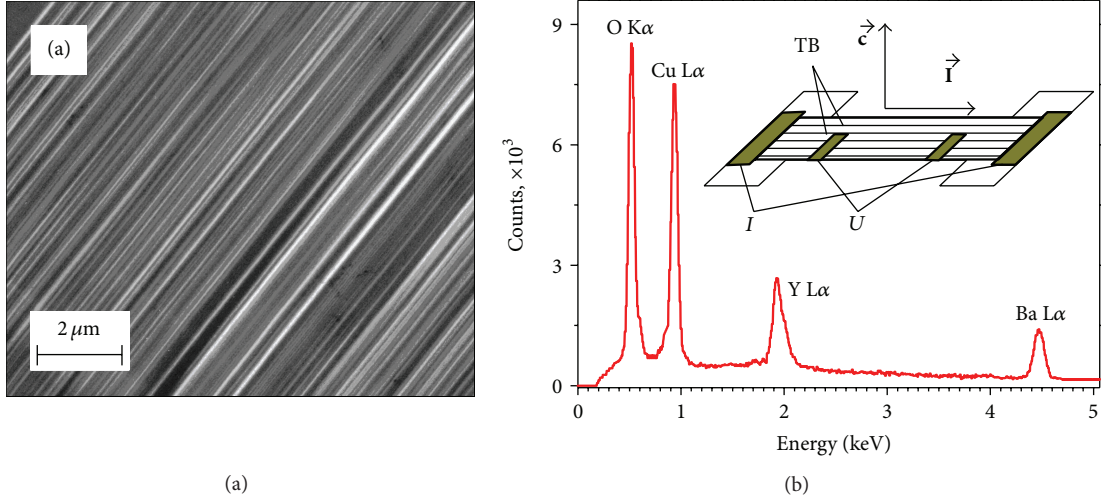


FIGURE 1: (a) Photograph of the section with unidirectional twin boundaries in the Al-doped crystal K2. (b) Main panel: Material composition in the as-grown pure crystal K1 revealed by energy-dispersive X-ray spectroscopy (probed area of $2 \times 2 \mu\text{m}^2$). Inset: Geometry of the experiment, see text for details.

the defect formation [24, 25]. As their concentration increases, the period of the domain structure decreases. As a consequence of this, neighboring microtwins overlap and a tweed-like structure results [25]. As it is evident from Figure 1(a), such a tweed-like structure is absent in the investigated crystal of $\text{YBa}_2\text{Cu}_{3-y}\text{Al}_y\text{O}_{7-\delta}$. This must be attributed to the low concentration of Al. We also note that the twin-to-twin distance in the Al-doped crystal K2 is a factor of 2-3 smaller than that in the pure crystal K1.

3. Results and Discussion

The temperature dependences of the electrical resistivity in the ab plane $\rho_{ab}(T)$ of crystals K1 and K2, measured before and after prolonged aging in air atmosphere, are shown in Figures 2(a) and 2(b), respectively. The superconducting transitions for the same samples are shown in $\rho_{ab}-T$ and $d\rho_{ab}/dT-T$ coordinates in the respective insets. One can see that in all the cases the dependences are quasimetallic. However, the ratio $\rho_{ab}(300 \text{ K})/\rho_{ab}(0 \text{ K})$ measured for the as-grown and aged samples has diminished from 64 to 39 and from 12 to 8 for crystals K1 and K2, respectively. Here, the value of $\rho_{ab}(0 \text{ K})$ was determined by extrapolating the linear section in $\rho_{ab}(T)$, as shown by the dashed lines in Figure 2. At the same time, the resistivity $\rho_{ab}(300 \text{ K})$ of crystals K1 and K2 has risen from 151 to 196 and from 421 to 453 $\mu\Omega\text{cm}$, accordingly. This has been accompanied by the respective reduction of their critical temperature from 91.75 to 90.83 and from 92.05 to 90.85 K. In our measurements, the critical temperature T_c was determined as that corresponding to the maximum in the dependence $d\rho_{ab}(T)/dT$. For both aged samples, the width of the superconducting transition, ΔT_c , has noticeably increased (from 0.3 and 0.5 to $\approx 1 \text{ K}$ for crystals K1 and K2, resp.), and the transition of crystal K2 has gained a stepwise shape. The measured and calculated parameters of the investigated samples are compiled in Table 1. Using the literature data for the dependence of T_c on the oxygen concentration [27],

one can arrive at the conclusion that in both aged crystals its content has insufficiently (by 1-2%) decreased and is within $\delta \leq 0.15$ [27]. The broadening of the resistive transitions for both crystals reflects a decrease in homogeneity of the investigated samples [9, 10, 12, 13], whereas the stepwise shape of the transition in the remeasurements on crystal K2 testifies that the phase segregation appeared in its volume [10, 12]. The latter assumption is supported by the presence of a series of peaks in the dependence $d\rho_{ab}(T)/dT$ of crystal K2. According to [9], such peaks correspond to T_c of different phases in the crystal volume. The absence of peaks for crystal K1 suggests that percolation pathways are likely to ensue for the current flow through the phase with a higher T_c [28].

As it follows from Figure 2 and Table 1, the relative change in the resistive parameters during the aging process is more pronounced for the pure crystal K1 than for the Al-doped K2. As the current I is applied parallel to TBs in all the samples, this difference cannot be caused by the enhanced density of TBs in crystal K2 exhibiting a smaller twin-to-twin distance. The observed increase of ρ_{ab} for the aged samples must be caused by a decrease of the density of the charge carriers or the appearance of effective scattering centers. This is also supported by the reduction of the ratio $\rho_{ab}(300 \text{ K})/\rho_{ab}(0 \text{ K})$. The role of such scattering centers may be played by an increasing number of vacancies that appeared in the aged samples and by a rise in nonstoichiometry of the compound, most likely owing to losses of oxygen. Along with increasing ρ_{ab} , as already mentioned above, a series of peaks have appeared in $d\rho_{ab}/dT$ of sample K2. This must assert the risen number of different phase inclusions [28] in the crystal volume. As is known [24], impurities of the 3-valent Al have a significantly smaller radius than the one that Cu has, thereby providing the centers for the defects formation. In these, aluminum atoms can form a specific octahedral environment of oxygen atoms [24] that, in turn, can facilitate the segregation of the conducting subsystem into several phases with different T_c . The presence of such

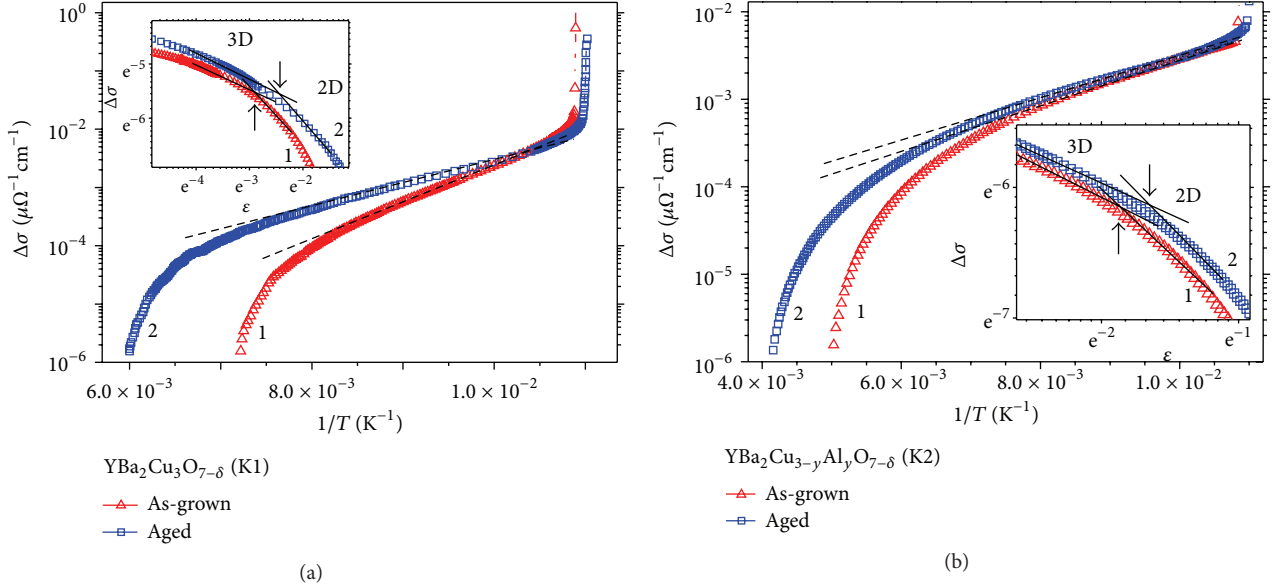


FIGURE 3: The temperature dependence of the excess conductivity $\Delta\sigma(T)$ in the ab plane of the single crystals (a) $\text{YBa}_2\text{Cu}_3\text{O}_{7-\delta}$ and (b) $\text{YBa}_2\text{Cu}_{3-y}\text{Al}_y\text{O}_{7-\delta}$ before and after long aging in air, in $\ln \Delta\sigma$ - $1/T$ (main panels) and $\ln \Delta\sigma$ - $\ln \varepsilon$ coordinates (insets). The dashed straight lines are fits by (2). In the insets, the solid straight lines are linear fits with slopes $\tan \alpha_{3D} \approx -0.5$ (3D regime) and $\tan \alpha_{2D} \approx -1$ (2D regime). The arrows show the 3D-2D crossover point. The numbering of the curves is the same as in Figure 2.

samples [13]. The fitting range of the experimental data can be substantially extended by introducing the factor $(1 - T/T^*)$. In this case, the excess conductivity turns out to be proportional to the density of superconducting carriers, $n_s \propto (1 - T/T^*)$, and inversely proportional to the number of pairs $\propto \exp(-\Delta_{ab}^*/kT)$ destroyed by thermal motion. Here T^* is regarded as the mean-field transition temperature to the PG regime, and the temperature range $T_c < T < T^*$, where the PG state exists, is determined by the rigidity of the order parameter phase. The latter, in turn, depends on the oxygen deficiency and the concentration of the doping element. Other specific mechanisms of the quasiparticle interaction, such as those caused by structural or kinematic anisotropy of the system, can also be relevant [32, 33]. The values of Δ_{ab}^* calculated by (2) for our samples are presented in Table 1. It is evident that the prolonged aging leads to the substantial suppression of the absolute value of the PG; namely, $\Delta_{ab1}^*/\Delta_{ab2}^* = 1.34$ and $\Delta_{ab1}^*/\Delta_{ab2}^* = 1.28$ for crystals K1 and K2, respectively.

As it follows from the main panels of Figure 3, with approaching T_c , a sharp rise in $\Delta\sigma(T)$ ensues. From the Aslamazov-Larkin theory [34], it is known that in the vicinity of T_c the excess conductivity is stipulated by the processes of fluctuational pairing of the charge carriers. The excess conductivity at $T > T_c$ for the two- (2D) and three-dimensional (3D) cases is determined by the following power-law dependences:

$$\Delta\sigma_{2D} = \frac{e^2}{16\hbar d} \varepsilon^{-1}, \quad (3)$$

$$\Delta\sigma_{3D} = \frac{e^2}{32\hbar\xi_c(0)} \varepsilon^{-1/2}, \quad (4)$$

where $\varepsilon = (T - T_c)/T_c$ is the reduced temperature, e is the electron charge, $\xi_c(0)$ is the coherence length along the axis c at $T \rightarrow 0$, and d is the characteristic dimension of the 2D layer.

To deduce the exponents determining the prevailing regime, the temperature dependences $\Delta\sigma(T)$ are plotted in $\ln \Delta\sigma$ - $\ln \varepsilon$ coordinates in the insets of Figure 3. From these plots, it is seen that, in the vicinity of T_c , both dependences can be fitted well by straight lines with a tilt angle $\tan \alpha_{3D} \approx -0.5$ corresponding to the exponent $-1/2$ in (4). This evidently asserts the 3D character of the fluctuational superconductivity in this temperature range. With a further increase of the temperature, the decrease of $\Delta\sigma$ speeds up essentially ($\tan \alpha_{2D} \approx -1$). This, in turn, can be treated as an indication of the dimensionality change in the fluctuation conductivity. As it follows from (3) and (4), in the 3D-2D crossover point,

$$\xi_c(0) \varepsilon_0^{-1/2} = \frac{d}{2}. \quad (5)$$

In this case, having deduced the value of ε_0 and using the literature data on the dependence of the lattice parameter on δ [35] ($d = 11.7 \text{ \AA}$), one can calculate $\xi_c(0)$. Such calculations show that after prolonged exposure the coherence length $\xi_c(0)$ has increased from 1.49 to 1.74 and from 2.32 to 2.54 \AA for crystals K1 and K2, respectively. This is accompanied by a shift of the 3D-2D crossover temperature, T_{3D-2D} , towards higher temperatures; see also Table 1 and Figure 3.

As a generalization of the obtained results, the observed changes in the three determinative temperatures are presented in the form of a chart in Figure 4. This sketch allows one to grasp the impact of aluminum doping and prolonged aging on the implementation of the different conductivity

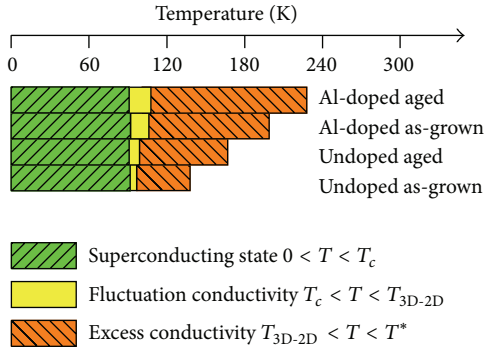


FIGURE 4: The impact of aluminum doping and prolonged aging on the implementation of the different conductivity regimes for the investigated single crystals of YBaCuO.

regimes in the investigated samples, in the entire temperature range. The three characteristic temperatures are the superconducting transition temperature T_c , the mean-field transition temperature to the pseudogap regime T^* , and the crossover temperature T_{3D-2D} for the dimensionality change in the power-law dependence of the excess conductivity. We leave more subtle subregions, such as those corresponding to the critical fluctuations and noninteger dimensionality, as they are beyond the scope of this work. From Figure 4 it follows that both the 6-year aging and aluminum doping in the investigated concentration suppress T_c very slightly (by less than 1%). At the same time, when combining both of these treatments, the temperature range for the PG state to ensue is essentially expanded (by a factor of 2-3) towards higher temperatures. The increase of T^* due to aluminum doping is accompanied by a worth noting rise in T_{3D-2D} (by about 10%), whereas T_{3D-2D} remains almost unchanged in process of aging for both investigated samples.

4. Conclusion

In conclusion, let us sum up the main results obtained in this work. A long exposure of the optimally doped single crystals of YBaCuO in air atmosphere has been found to lead to an incomplete degradation of their conductive properties and to the appearance of effective scattering centers for the charge carriers. The introduction of Al impurities assists a partial slowdown of the degradation of the conducting properties in process of aging of the samples. The excess conductivity $\Delta\sigma(T)$ of the pure and Al-doped single crystals of YBaCuO obeys the exponential dependence in the broad temperature range $T_c < T < T^*$ and, in the case of approaching T_c , can be described well within the Aslamazov-Larkin theoretical model. The prolonged exposure of the samples leads to an essential broadening of the temperature range for the pseudogap state in the ab plane to ensue, thus narrowing the linear section in the dependence $\rho_{ab}(T)$. Along with this, indications of the phase segregation in the volume of the Al-doped sample have been observed. These become apparent via the presence of additional peaks in $d\rho_{ab}(T)/dT$ at temperatures close to the superconducting transition temperature.

Conflict of Interests

The authors declare that there is no conflict of interests.

Acknowledgments

Oleksandr V. Dobrovolskiy thanks Michael Huth for providing access to the scanning electron microscope and Evgeniya Begun for her help with EDX measurements. This work was supported in part by the European Commission within the Seventh Framework Programme (FP7), Project no. 247556. Oleksandr V. Dobrovolskiy acknowledges the Deutsche Forschungsgemeinschaft for financial support through Grant no. DO 1511/2-1.

References

- [1] J. Bednorz and K. Müller, "Possible high- T_c superconductivity in the Ba-La-Cu-O system," *Zeitschrift für Physik B*, vol. 64, pp. 189–193, 1986.
- [2] T. Timusk and B. Statt, "The pseudogap in high-temperature superconductors: an experimental survey," *Reports on Progress in Physics*, vol. 62, no. 1, pp. 61–122, 1999.
- [3] T. Tohyama and S. Maekawa, "Angle-resolved photoemission in high T_c cuprates from theoretical viewpoints," *Superconductor Science and Technology*, vol. 13, no. 4, pp. R17–R32, 2000.
- [4] M. L. Kulić, "Interplay of electron-phonon interaction and strong correlations: the possible way to high-temperature superconductivity," *Physics Reports*, vol. 338, no. 1-2, pp. 1–264, 2000.
- [5] J. L. Tallon and J. W. Loram, "Doping dependence of T^* —what is the real high- T_c phase diagram?" *Physica C*, vol. 349, no. 1-2, pp. 53–68, 2001.
- [6] H. G. Luo, Y. H. Su, and T. Xiang, "Scaling analysis of normal-state properties of high-temperature superconductors," *Physical Review B*, vol. 77, Article ID 014529, 2008.
- [7] C. V. Varanasi, J. Burke, H. Wang, J. H. Lee, and P. N. Barnes, "Thick YBa₂Cu₃O_{7-x} + BaSnO₃ films with enhanced critical current density at high magnetic fields," *Applied Physics Letters*, vol. 93, no. 9, Article ID 092501, 2008.
- [8] J. D. Jorgensen, S. Pei, P. Lightfoot, H. Shi, A. P. Paulikas, and B. W. Veal, "Time-dependent structural phenomena at room temperature in quenched YBa₂Cu₃O_{6.41}. Local oxygen ordering and superconductivity," *Physica C*, vol. 167, no. 5-6, pp. 571–578, 1990.
- [9] R. V. Vovk, M. A. Obolenskii, A. A. Zavgorodniy, I. L. Goulatis, V. I. Beletskii, and A. Chroneos, "Structural relaxation, metal-to-insulator transition and pseudo-gap in oxygen deficient HoBa₂Cu₃O_{7-δ} single crystals," *Physica C*, vol. 469, pp. 203–206, 2009.
- [10] R. V. Vovk, Z. F. Nazyrov, M. A. Obolenskii, I. L. Goulatis, A. Chroneos, and V. M. Pinto Simoes, "Phase separation in oxygen deficient HoBa₂Cu₃O_{7-δ} single crystals: effect of high pressure and twin boundaries," *Philosophical Magazine*, vol. 91, no. 17, pp. 2291–2302, 2011.
- [11] S. Sadewasser, J. S. Schilling, A. P. Paulikas, and B. W. Veal, "Pressure dependence of T_c to 17 GPa with and without relaxation effects in superconducting YBa₂Cu₃O_x," *Physical Review B*, vol. 61, no. 1, pp. 741–749, 2000.
- [12] R. V. Vovk, G. Y. Khadzhai, Z. F. Nazyrov, I. L. Goulatis, and A. Chroneos, "Relaxation of the normal electrical

- resistivity induced by high-pressure in strongly underdoped $\text{YBa}_2\text{Cu}_3\text{O}_{7-\delta}$ single crystals,” *Physica B*, vol. 407, pp. 4470–4472, 2012.
- [13] R. V. Vovk, N. R. Vovk, G. Y. Khadzhai, I. L. Goulatis, and A. Chroneos, “Effect of high pressure on the electrical resistivity of optimally doped $\text{YBa}_2\text{Cu}_3\text{O}_{7-\delta}$ single crystals with unidirectional planar defects,” *Physica B*, vol. 422, pp. 33–35, 2013.
- [14] Z. Li, H. Wang, N. Yang, X. Jin, and L. Shen, “Influence of air components on the stability of $\text{YBa}_2\text{Cu}_3\text{O}_{7-\delta}$,” *Journal of the Chinese Ceramic Society*, vol. 18, no. 6, pp. 555–560, 1990.
- [15] B. Martínez, F. Sandiumenge, S. Piñol, N. Vilalta, J. Fontcuberta, and X. Obradors, “Aging of critical currents and irreversibility line in melt textured $\text{YBa}_2\text{Cu}_3\text{O}_{7-\delta}$,” *Applied Physics Letters*, p. 772, 1995.
- [16] K. Schlesier, H. Huhtinen, S. Granroth, and P. Paturi, “An aging effect and its origin in GdBCO thin films,” *Journal of Physics*, vol. 234, no. 1, Article ID 012036, 2010.
- [17] Q.-R. Feng, X. Zhu, S.-Q. Feng, H. Zhang, and Z.-Z. Gan, “Effect of time aging on the properties of Ag-doped YBaCuO superconductors,” *Superconductor Science and Technology*, vol. 6, no. 10, pp. 715–720, 1993.
- [18] R. V. Vovk, Z. F. Nazyrov, I. L. Goulatis, and A. Chroneos, “Metal-to-insulator transition in $\text{Y}_{1-x}\text{Pr}_x\text{Ba}_2\text{Cu}_3\text{O}_{7-\delta}$ single crystals with various praseodymium contents,” *Physica C*, vol. 485, pp. 89–91, 2013.
- [19] R. V. Vovk, M. A. Obolenskii, A. V. Bondarenko et al., “Transport anisotropy and pseudo-gap state in oxygen deficient $\text{ReBa}_2\text{Cu}_3\text{O}_{7-\delta}$ (Re = Y, Ho) single crystals,” *Journal of Alloys and Compounds*, vol. 464, no. 1-2, pp. 58–66, 2008.
- [20] M. Z. Cieplak, G. Xiao, C. L. Chien et al., “Incorporation of gold into $\text{YBa}_2\text{Cu}_3\text{O}_7$: structure and T_c enhancement,” *Physical Review B*, vol. 42, no. 10, pp. 6200–6208, 1990.
- [21] D. A. Lotnyk, R. V. Vovk, M. A. Obolenskii et al., “Evolution of the Fishtail-effect in pure and Ag-doped MG-YBCO,” *Journal of Low Temperature Physics*, vol. 161, no. 3-4, pp. 387–394, 2010.
- [22] R. B. Van Dover, L. F. Schneemeyer, J. V. Waszczak, D. A. Rudman, J. Y. Juang, and J. A. Cutro, “Extraordinary effect of aluminum substitution on the upper critical field of $\text{YBa}_2\text{Cu}_3\text{O}_7$: structure and T_c ,” *Physical Review B*, vol. 39, no. 4, pp. 2932–2935, 1989.
- [23] B. Oh, K. Char, A. D. Kent et al., “Upper critical field, fluctuation conductivity, and dimensionality of $\text{YBa}_2\text{Cu}_3\text{O}_{7-x}$,” *Physical Review B*, vol. 37, no. 13, pp. 7861–7864, 1988.
- [24] R. V. Vovk, M. A. Obolenskii, Z. F. Nazyrov, I. L. Goulatis, A. Chroneos, and V. M. Pinto Simoes, “Electro-transport and structure of 1-2-3 HTSC single crystals with different plane defects topologies,” *Journal of Materials Science*, vol. 23, pp. 1255–1259, 2012.
- [25] G. Lacayo, G. Kästner, and R. Herrmann, “Twin to tweed transition in $\text{YBa}_2\text{Cu}_3\text{O}_{7-\delta}$ by substitution of Al for Cu,” *Physica C*, vol. 192, no. 1-2, pp. 207–214, 1992.
- [26] A. V. Bondarenko, V. A. Shklovskij, M. A. Obolenskii et al., “Resistivity investigations of plastic vortex creep in $\text{YBa}_2\text{Cu}_3\text{O}_{6.95}$ crystals,” *Physical Review B*, vol. 58, no. 5, pp. 2445–2447, 1998.
- [27] P. Schleger, W. Hardy, and B. Yang, “Thermodynamics of oxygen in $\text{YBa}_2\text{Cu}_3\text{O}_x$ between 450°C and 650°C,” *Physica C*, vol. 176, pp. 261–273, 1991.
- [28] R. V. Vovk, M. A. Obolenskii, A. A. Zavgorodniy et al., “Effect of high pressure on the fluctuation conductivity and the charge transfer of $\text{YBa}_2\text{Cu}_3\text{O}_{7-\delta}$ single crystals,” *Journal of Alloys and Compounds*, vol. 453, no. 1-2, pp. 69–74, 2008.
- [29] M. V. Sadovskii, I. A. Nekrasov, E. Z. Kuchinskii, T. Pruschke, and V. I. Anisimov, “Pseudogaps in strongly correlated metals: a generalized dynamical mean-field theory approach,” *Physical Review B*, vol. 72, no. 15, Article ID 155105, 2005.
- [30] R. V. Vovk, M. A. Obolenskii, A. A. Zavgorodniy, D. A. Lotnyk, and K. A. Kotvitskaya, “Temperature dependence of the pseudogap in aluminum and praseodymium-doped $\text{YBa}_2\text{Cu}_3\text{O}_{7-\delta}$ single crystals,” *Physica B*, vol. 404, no. 20, pp. 3516–3518, 2009.
- [31] E. Babaev and H. Kleinert, “Nonperturbative XY-model approach to strong coupling superconductivity in two and three dimensions,” *Physical Review B*, vol. 59, no. 18, pp. 12083–12089, 1999.
- [32] V. M. Apalkov and M. E. Portnoi, “Two-phonon scattering of magnetorotons in fractional quantum Hall liquids,” *Physical Review B*, vol. 66, no. 12, Article ID 121303, 2002.
- [33] P. J. Curran, V. V. Khotkevych, S. J. Bending, A. S. Gibbs, S. L. Lee, and A. P. MacKenzie, “Vortex imaging and vortex lattice transitions in superconducting Sr_2RuO_4 single crystals,” *Physical Review B*, vol. 84, no. 10, Article ID 104507, 2011.
- [34] L. G. Aslamasov and A. I. Larkin, “The influence of fluctuation pairing of electrons on the conductivity of normal metal,” *Physics Letters A*, vol. 26, no. 6, pp. 238–239, 1968.
- [35] G. D. Chryssikos, E. I. Kamitsos, J. A. Kapoutsis et al., “X-ray diffraction and infrared investigation of $\text{RBa}_2\text{Cu}_3\text{O}_7$ and $\text{R}_{0.5}\text{Pr}_{0.5}\text{Ba}_2\text{Cu}_3\text{O}_7$ compounds (R = Y and lanthanides),” *Physica C*, vol. 254, no. 1-2, pp. 44–62, 1995.

Research Article

Oxygen Defects Mediated Magnetism of Ni Doped ZnO

W. J. Liu,¹ X. D. Tang,² Z. Tang,² W. Bai,² and N. Y. Tang¹

¹ Shanghai University of Electric Power, 2588 Pingyang Road, Shanghai 200090, China

² East China Normal University, 500 Dongchuan Road, Shanghai 200241, China

Correspondence should be addressed to W. J. Liu; liuwj5500@gmail.com

Received 23 July 2013; Revised 2 September 2013; Accepted 16 September 2013

Academic Editor: Xuan Luo

Copyright © 2013 W. J. Liu et al. This is an open access article distributed under the Creative Commons Attribution License, which permits unrestricted use, distribution, and reproduction in any medium, provided the original work is properly cited.

Ni doped ZnO nanoparticles were synthesized by a solution route and annealed in O₂, air, and Ar, respectively. X-ray diffraction and X-ray photoelectron spectroscopy measurements show that the samples possess typical wurtzite structure and have no other impurity phases. Magnetization loops for ZnO samples were measured and clearly show typical ferromagnetic saturation behavior. With the defect analysis based on photoluminescence spectroscopy, the effect of defects on the nature and origin of ferromagnetism was investigated. The results suggest that oxygen vacancies, especially single ionized oxygen vacancies, play a crucial role in mediating ferromagnetism in the Ni doped ZnO.

1. Introduction

Diluted magnetic oxide semiconductors (DMOSs) have gained much attention recently due to the possibility to control spin and charge simultaneously for future spintronics [1, 2]. These oxide semiconductors with a wide band gap are optically transparent in visible region and important for the development of spin related optoelectronic devices. After the theoretical prediction by Dietl et al. suggesting the existence of room temperature ferromagnetism (FM) in doped ZnO, the system has been extensively studied [3, 4]. Remarkable progress has been made in the realization of transition metal (TM) doped ZnO with Curie temperature (T_c) at or above room temperature (RT). It was also reported that even doping “nonmagnetic” atoms such as Cu or Bi leads to RT FM in ZnO [5, 6]. More recently, FM had been observed in undoped ZnO, which opened an extensive debate on the origin of FM [7, 8]. Therefore, some researches suggested that induced FM is due to oxygen defects in ZnO, not TM ions or secondary phases. Although the origin of FM in TM doped and undoped ZnO has not been fully understood so far, oxygen (or Zn) defects are broadly recognized as an important reason for the FM behavior of doped and undoped ZnO, which is also consistent with our previous work on FM of undoped ZnO [9].

In the present work, we have focused our attention on further research of the role of oxygen (or Zn) defects by investigating the effect of different annealing atmospheres on

the FM properties of Ni doped ZnO nanoparticles based on an analysis of photoluminescence (PL) spectroscopy.

2. Experimental

2.1. Preparation of Ni Doped ZnO Nanoparticles. Ni doped ZnO nanoparticles were prepared by a solution method. A total of 0.01 mol of zinc acetate (Zn(AC)₂·2H₂O) and Nickel acetate (Ni(AC)₂·4H₂O) in the chosen atomic ratios were dissolved in 200ml deionized water as the precursor together with 0.01 mol methenamine (C₆H₁₂N₄, HMT). Then they were mixed under vigorous stirring for 30 min in a glass beaker. Before growth, a glass substrate was cleaned carefully and put into the glass beaker. The growth time and temperature were 24 h and 95°C, respectively. After growth, the substrate was taken out the solution, thoroughly rinsed with deionized water, treated in an ultrasonic water bath for 10 min, and dried in air at room temperature. To investigate the influence of defects on the inducing magnetic moment, the resulting sample was divided into three parts for the followed anneal at 800°C for 30 min in Ar, air, and O₂, respectively.

2.2. Characterization. The structure of Ni doped ZnO nanoparticles was determined by X-ray diffraction (XRD) with Cu *K*_α radiation ($\lambda = 0.1542$ nm) at RT. The effective concentration and binding state of the ions in the

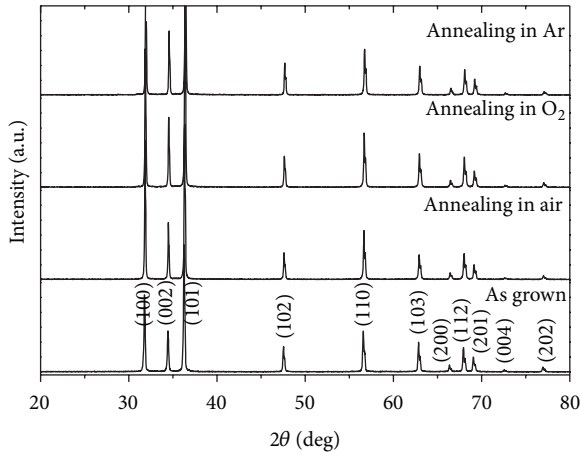


FIGURE 1: X-ray diffraction of Ni doped ZnO samples as grown and thermal annealed in different atmosphere.

nanostructures were characterized with X-ray photoelectron spectroscopy (XPS) (ESCA-LAB 250, Thermo-VG Scientific). The optical properties were characterized by photoluminescence (JobinYvon-800 HR). The magnetic properties were investigated by means of a SQUID magnetometer (MPMS, Quantum Design-PPMS 9).

3. Results and Discussion

3.1. Microstructure. The structure of Ni doped ZnO particles was characterized by XRD at RT, as shown in Figure 1. No other diffraction peaks besides those of wurtzite ZnO can be observed. Thus, it was demonstrated that the samples possess the typical wurtzite structure and no impurity phases are present.

3.2. XPS Analysis. X-ray photoelectron spectroscopy is the most useful tool to analyze the surface valence states of the elements in a material. To further investigate the composition and structure of the prepared particles, XPS spectra of Ni doped ZnO sample were measured and are shown in Figure 2.

An extended scan is reproduced in Figure 2(a). The Zn2p3 spectrum exhibits an asymmetry feature, indicating the possibility of existence of multicomponent Zn. Gaussian resolving is performed and two peaks obtained were centered at 1020.93 and 1022.42 eV (see Figure 2(b)). The peak centered at 1020.93 eV corresponds to the binding energies of Zn2p3 of undoped ZnO. The peak centered at 1022.42 eV is attributed to the Zn2p3 of Ni doped ZnO. This increase of binding energy is due to the substitution of parts of the lattice Zn in ZnO by Ni²⁺ ions with the larger ionic radius and the formation of Zn–Ni bonding structure.

To investigate the distributing of Ni element, gaussian resolving is also performed on the Ni2p spectrum. The peaks of Ni 2p3/2 and Ni 2p1/2 core levels are found to be centered at 855.54 and 873.1 eV, respectively, whereas the corresponding satellite structures are clearly observed at 861.3 and 878.7 eV. The peak positions depend on the

local structure of the Ni atoms and provide the information about the chemical state. The Ni 2p3/2 (855.54 eV) position is quite different from that of metallic Ni (852.7 eV), NiO (853.8 eV), and Ni₂O₃ (856.7 eV). The absence of Ni metallic clusters can also be explained on the basis of energy difference between Ni 2p3/2 and Ni 2p1/2 core levels. For Ni doped ZnO, the difference is 17.56 eV, which is different from the value of metallic Ni (17.27 eV). This energy difference for NiO (17.49 eV) is very close to the observed (17.56 eV) value, which gives the evidence that Ni is in +2 valance state; however, the presence of NiO can be ruled out as NiO is antiferromagnetic (TN 520 K), whereas in this case, room temperature ferromagnetism is observed. Furthermore, the shape of peaks for Ni metallic with satellites structure is narrow and different from the observed spectrum of Ni doped ZnO nanorods. These results give evidence that Ni ions with valence +2 are successfully substituted into tetrahedral sites of the ZnO wurtzite structure without forming any detectable impurity phase, such as Ni metal, Ni₂O₃, and NiO. The atomic concentration of Ni is about 2.90%.

The XPS spectrum of O1s is asymmetric (see Figure 2(d)), indicating the presence of multicomponent oxygen species in the near-surface region. It can be fitted with three components, which are centered at 529.92 eV, 531.2 eV, and 531.74 eV, respectively. The peak at about 529.92 eV is attributed to the ZnNiO crystal lattice oxygen. The peak at about 531.2 eV is associated with oxygen-deficient regions in the ZnNiO matrix. The peak at about 531.74 eV is due to the chemisorbed oxygen of the surface hydroxyl, –CO₃, adsorbed H₂O, or adsorbed O₂ [10–12].

3.3. Photoluminescence Properties. To investigate the presence of defects, the RT PL spectra of Ni doped ZnO as grown and annealed at three different atmospheres are shown in Figure 3(a). Each spectrum displays ultraviolet (UV) near band-edge (NBE) emission. It is well known that, at RT, ZnO typically exhibits UV band-edge emission and broad visible emissions at green, orange, yellow, and red spectral bands. The UV band-edge emission is attributed to free excitonic emission. It is reasonable to assume that this PL mechanism is the same for all our investigated Ni doped ZnO samples. We observed the UV near-band-edge emission peak at 380–400 nm. Here, we only report data for visible emission, which is referred to as deep-level emission and attributed to recombination of electrons deeply trapped in oxygen/Zn vacancies and interstitials, with photo-generated holes.

Many reports have focused on the origin of the PL in doped and undoped ZnO. There are three peaks in the visible band, 527 nm, 575 nm, and 657 nm. The green emission (527 nm) is generally attributed to the recombination of electrons trapped in single ionized oxygen vacancies (V_o^+) with photo generated holes [13, 14]. The green emission (575 nm) is related to the doubly ionized oxygen vacancy (V_o^{++}) [15–17]. The red emission around 657 nm originates from the intrinsic defects of oxygen interstitials (O_i) [18–20], which act as traps for photo-generated holes.

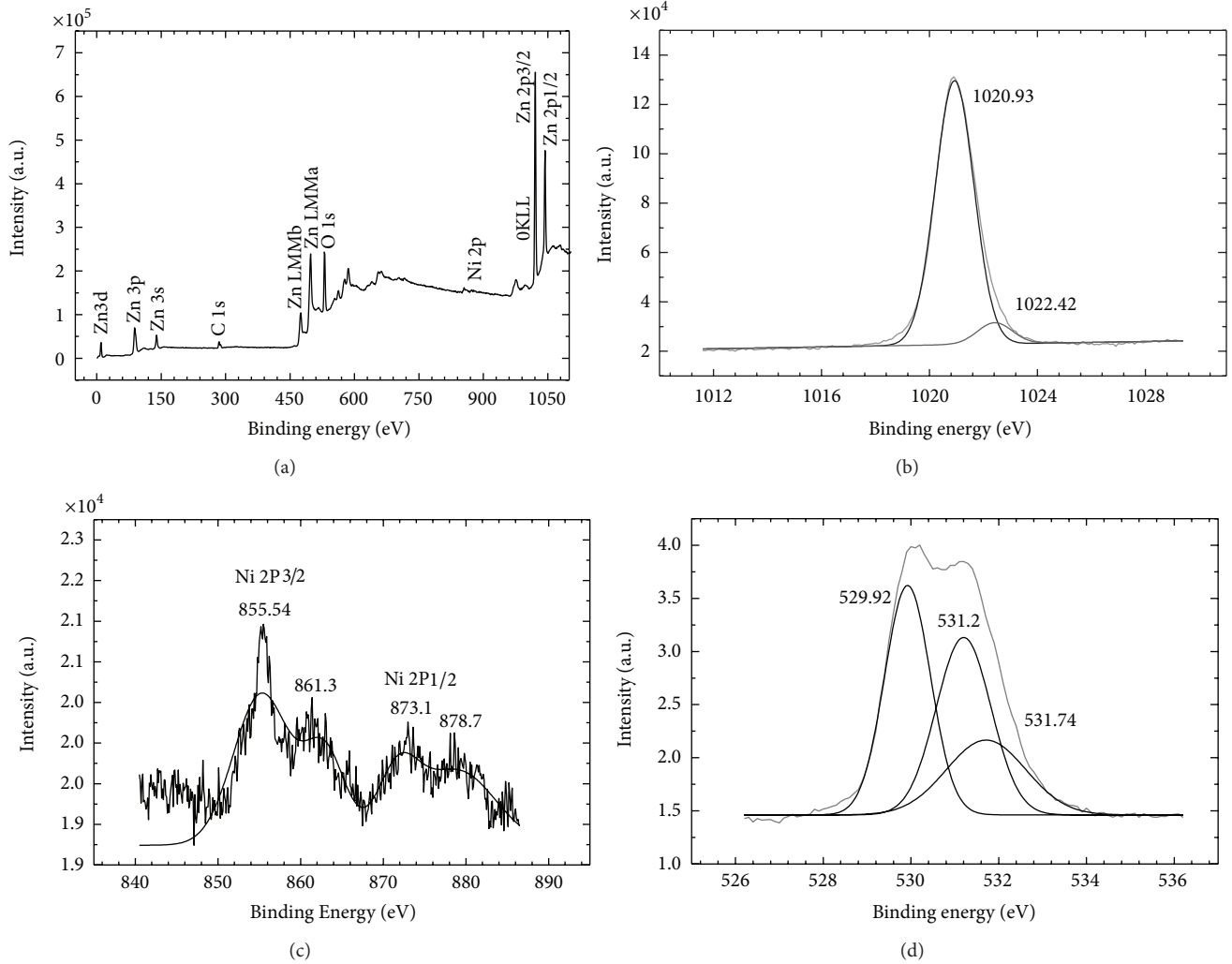


FIGURE 2: XPS spectra of as-grown Ni-doped ZnO samples: (a) Extended scan; (b) Zn2p_{3/2} spectrum; (c) Ni2p_{3/2} spectrum; (d) O1s spectrum. (The gray lines represent experimental results and the black solid curves are Gaussian fits of the components).

Gaussian fitting is performed on each spectrum to investigate the distributing of the above three defects, which is shown in Figure 3(b). Figure 4 displays the contents of oxygen related defects in Ni-doped ZnO samples as-grown and postannealed in different atmospheres (O₂, air, and Ar).

During the annealing process in Ar and air, oxygen easily escapes from the ZnO particles, the concentration of oxygen vacancies (V_o^+ and V_o^{++}) increases, and the concentration of O_i decreases. After annealing in O₂, the oxygen vacancies in the sample are filled to a large extent and the concentration of oxygen interstitials has increased. At the same time, the relative contents of V_o^+ increases due to the fact that part of V_o^{++} have been transformed into V_o^+ during the annealing process.

3.4. Magnetic Properties. Magnetization loops for the samples in capsules were measured at 300 K using a VSM magnetometer and the M-H curves are shown in Figure 5. The actual magnetization of the samples was determined by subtracting the diamagnetic contribution of the capsule and substrate

from the raw data. Our experimental results presented indeed show that all the samples are ferromagnetic at RT. The M-H curves clearly show that the typical ferromagnetic saturation behavior. Particularly, it is observed that the post-annealing in different atmospheres does not change the essential FM of the samples but does change significantly the saturated magnetic moments (M_s) of the samples.

3.5. Discussion. The mechanism of intrinsic FM in TM-doped oxides still remains controversial, whether it is an intrinsic or extrinsic property of these materials. A diversity of theories has been proposed. For instance, the magnetism of the TM-doped ZnO has been attributed to ferromagnetic coupling of the local moment of TM dopants through the carrier-mediated Ruderman-Kittel-Kasuya-Yosida (RKKY) interaction [21], indirect double-exchange [22, 23] or superexchange [24], and so forth. There are even proposals that the observed FM originates from the local magnetic moment of defects such as the Zn vacancies [25] or O vacancies [26–29].

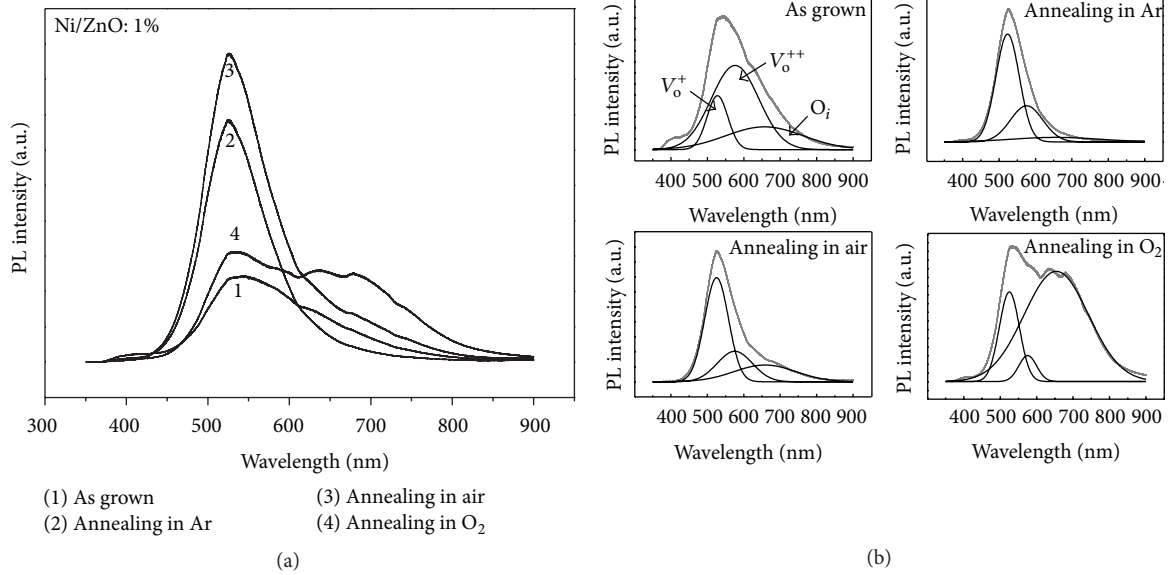


FIGURE 3: RT photoluminescence spectra of Ni doped ZnO samples as grown and annealed in different atmosphere (a) and Gaussian fit of each PL spectrum (b) (The gray lines are the experimental results and the black solid curves are Gaussian fits).

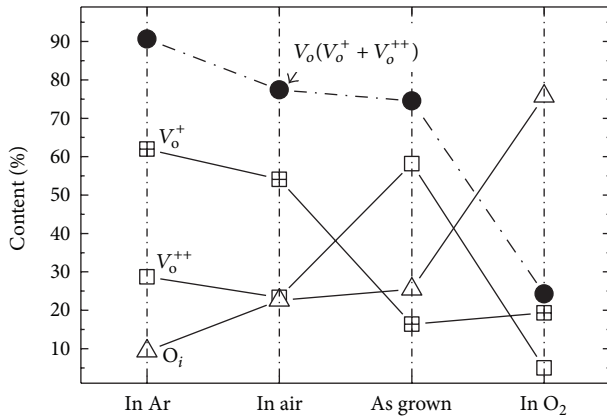


FIGURE 4: The contents of oxygen related defects (V_o⁺, V_o⁺⁺ and O_i) in as grown Ni doped ZnO nanoparticles, and samples with thermal annealing in O₂, air, and Ar, respectively.

In the present work, XRD and XPS results clearly demonstrate that the samples have a single wurtzite phase and there is no indication of additional phases, such as the Ni magnetic precipitation. So, we expect that FM is from an intrinsic exchange interaction of magnetic moments in Ni doped ZnO. Although the exact mechanism of intrinsic FM in Ni doped oxides is still under debate, defects have greatly been suggested to play an important role in the magnetic origin in the Ni doped ZnO system. As the postannealing is expected to have remarked effects on the defects rather than on the TM dopants, the combination of the present defects analyses based on the PL and the magnetic measurements provides a good opportunity to clarify the physical nature of the local magnetic moment.

In the PL results, Zn vacancies and interstitials were not observed in the prepared Ni doped ZnO system. So the

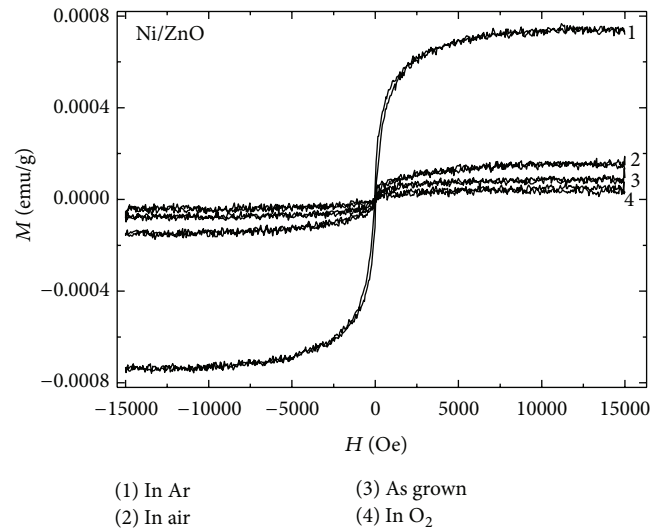


FIGURE 5: Magnetic hysteresis of Ni doped ZnO samples as grown and postannealed in different atmospheres (O₂, air, and Ar).

contributions of the observed oxygen defects on FM will be discussed below.

From Figure 5 it is observed that the saturated magnetic moment increases after annealing in Ar and air but decreases after annealing in O₂. We compared the saturated magnetic moments with the optical spectroscopic intensities originated from the oxygen vacancies in two charge states and oxygen interstitials (Figure 4). A definitely positive correlation between the M_s and the intensity of V_o (V_o⁺ and V_o⁺⁺) is observed, while a pronounced negative correlation between the M_s and the intensity of O_i can be seen. These results indicate that the observed three different defects may make different contributions to FM and that oxygen vacancies and

its related defect complexes play an essential role in the Ni doped ZnO system. As the annealing in different atmospheres does not change the concentration of the Ni dopants, it is expected that the dominant differences of FM introduced by annealing among the samples are either the concentrations or the charge states of the oxygen related defects, such as oxygen vacancies (V_o) and V_o -Ni complexes.

Theoretical and experimental studies have later confirmed that ferromagnetism in transition metal doped ZnO system, especially in ZnO thin film, is genuine and commonly believed to be due to an exchange interaction between magnetic moments localized at the TM sites mediated by free charge carriers. And, the magnetic moment can actually be mediated by tuning the concentration of lattice defects, as well as that of the dopants [30]. In the present ZnO:Ni samples, there may coexist two different mechanisms in response to the observed magnetism. There is an indirect RKKY interaction among the magnetic dopants/defects, which is always ferromagnetic in the short-range regime. In addition, there is the antiferromagnetic superexchange interaction via the O anions. The observed magnetism depends on the competition of these two mechanisms. With increasing the oxygen vacancies, the antiferromagnetic superexchange is suppressed so that the positive correlation between the M_s and the intensity of oxygen vacancy is observed. In any sense, based on the present results, we suggest that in addition to the magnetic doping effect, oxygen vacancies, especially V_o^+ , play an essential role in the magnetic origin for Ni doped ZnO. The role of oxygen defects in mediating the FM in TM doped ZnO still needs further theoretical and experimental research.

4. Conclusion

In summary, Ni doped ZnO nanoparticles have been prepared with a solution method. The structure and the surface valence states of the elements in the samples were studied in detail. To investigate the influence of the defects on the inducing magnetic, the particles are annealed in O_2 , air, and Ar, respectively. RT PL spectra were measured to facilitate an investigation of the defects. Magnetization loops for the samples were measured at 300 K and clearly show typical ferromagnetic saturation behavior. A combination of results from the defects analyses based on the PL and the magnetic measurements suggest that oxygen vacancies, especially singly ionized oxygen vacancies, play a crucial role in mediating ferromagnetism in the Ni doped ZnO system.

Conflict of Interests

All the authors declare that they do not have any conflict of interests.

Acknowledgments

The work is supported by the National Science Foundation of China (Grant no. 61076089), the Shanghai Natural Science Foundation (Grant no. B10ZR1412400), and the National Natural Science Foundation (Grant no. 61204105).

References

- [1] G. A. Prinz, "Magnetoelectronics," *Science*, vol. 282, no. 5394, pp. 1660–1663, 1998.
- [2] S. A. Wolf, D. D. Awschalom, R. A. Buhrman et al., "Spintronics: a spin-based electronics vision for the future," *Science*, vol. 294, no. 5546, pp. 1488–1495, 2001.
- [3] T. Dietl, H. Ohno, F. Matsukura, J. Cibert, and D. Ferrand, "Zener model description of ferromagnetism in zinc-blende magnetic semiconductors," *Science*, vol. 287, no. 5455, pp. 1019–1022, 2000.
- [4] S. W. Jung, S. J. An, G. C. Yi et al., "Ferromagnetic properties of $Zn_{1-x}Mn_xO$ epitaxial thin films," *Applied Physics Letters*, vol. 80, article 4561, 2002.
- [5] C. Xu, J. Chun, D. Kim et al., "Structural characterization and low temperature growth of ferromagnetic Bi-Cu codoped ZnO bicrystal nanowires," *Applied Physics Letters*, vol. 91, Article ID 153104, 2007.
- [6] T. S. Herng, S. P. Lau, S. F. Yu, J. S. Chen, and K. S. Teng, "Zn-interstitial-enhanced ferromagnetism in Cu-doped ZnO films," *Journal of Magnetism and Magnetic Materials*, vol. 315, no. 2, pp. 107–110, 2007.
- [7] D. Q. Gao, Z. H. Zhang, J. L. Fu, Y. Xu, J. Qi, and D. S. Xue, "Room temperature ferromagnetism of pure ZnO nanoparticles," *Journal of Applied Physics*, vol. 105, Article ID 113928, 2009.
- [8] B. B. Straumal, A. A. Mazilkin, S. G. Protasova et al., "Magnetization study of nanograined pure and Mn-doped ZnO films: formation of a ferromagnetic grain-boundary foam," *Physical Review B*, vol. 79, no. 20, Article ID 205206, 2009.
- [9] W. Liu, W. Li, Z. Hu, Z. Tang, and X. Tang, "Effect of oxygen defects on ferromagnetic of undoped ZnO," *Journal of Applied Physics*, vol. 110, no. 1, Article ID 013901, 2011.
- [10] S. Asbrink, A. Wařkowska, L. Gerward, J. Staun Olsen, and E. Talik, "High-pressure phase transition and properties of spinel $ZnMn_2O_4$," *Physical Review B*, vol. 60, no. 18, Article ID 12656, 1999.
- [11] J. H. Li, D. Z. Shen, J. Y. Zhang et al., "Magnetism origin of Mn-doped ZnO nanoclusters," *Journal of Magnetism and Magnetic Materials*, vol. 302, pp. 118–121, 2006.
- [12] Y. Liu, S. H. Yang, Y. L. Zhang, and D. H. Bao, "Influence of annealing temperature on structural, optical and magnetic properties of Mn-doped ZnO thin films prepared by sol-gel method," *Journal of Magnetism and Magnetic Materials*, vol. 321, pp. 3406–3410, 2009.
- [13] S. Baek, J. Song, and S. Lim, "Improvement of the optical properties of ZnO nanorods by Fe doping," *Physica B*, vol. 399, no. 2, pp. 101–104, 2007.
- [14] C. Y. Lin, W. H. Wang, C.-S. Lee, K. W. Sun, and Y. W. Suen, "Magnetophotoluminescence properties of Co-doped ZnO nanorods," *Applied Physics Letters*, vol. 94, Article ID 151909, 2009.
- [15] A. Van Dijken, E. A. Meulenkaamp, D. Vanmaekelbergh, and A. Meijerink, "Luminescence of nanocrystalline ZnO particles: the mechanism of the ultraviolet and visible emission," *Journal of Luminescence*, vol. 87, pp. 454–456, 2000.
- [16] A. K. Srivastava, M. Deepa, N. Bahadur, and M. S. Goyat, "Influence of Fe doping on nanostructures and photoluminescence of sol-gel derived ZnO," *Materials Chemistry and Physics*, vol. 114, no. 1, pp. 194–198, 2009.
- [17] K. Vanheusden, C. H. Seager, W. L. Warren, D. R. Tallant, and J. A. Voigt, "Correlation between photoluminescence and oxygen

- vacancies in ZnO phosphors,” *Applied Physics Letters*, vol. 68, no. 3, pp. 403–405, 1996.
- [18] X. L. Wu, G. G. Siu, C. L. Fu, and H. C. Ong, “Photoluminescence and cathodoluminescence studies of stoichiometric and oxygen-deficient ZnO films,” *Applied Physics Letters*, vol. 78, article 2285, 2001.
- [19] B. Panigrahy, M. Aslam, D. Shanker Misra, M. Ghosh, and D. Bahadur, “Defect-Related Emissions and Magnetization Properties of ZnO Nanorods,” *Advanced Functional Materials*, vol. 20, pp. 1161–1165, 2010.
- [20] S. A. Studenikin, N. Golego, and M. Cocivera, “Fabrication of green and orange photoluminescent, undoped ZnO films using spray pyrolysis,” *Journal of Applied Physics*, vol. 84, no. 4, pp. 2287–2294, 1998.
- [21] P. Bruno and C. Chappert, “Oscillatory coupling between ferromagnetic layers separated by a nonmagnetic metal spacer,” *Physical Review Letters*, vol. 67, no. 12, pp. 1602–1605, 1991.
- [22] C. Zener, “Interaction between the d -shells in the transition metals—II. Ferromagnetic compounds of manganese with perovskite structure,” *Physical Review*, vol. 82, pp. 403–405, 1951.
- [23] P. W. Anderson and H. Hasegawa, “Considerations on double exchange,” *Physical Review*, vol. 100, no. 2, pp. 675–681, 1955.
- [24] H. Katayama-Yoshida, K. Sato, T. Fukushima et al., “Theory of ferromagnetic semiconductors,” *Physica Status Solidi A*, vol. 204, no. 1, pp. 15–32, 2007.
- [25] W. S. Yan, Z. H. Sun, and Q. H. Liu, “Zn vacancy induced room-temperature ferromagnetism in Mn-doped ZnO,” *Applied Physics Letters*, vol. 91, Article ID 062113, 2007.
- [26] C. H. Patterson, “Role of defects in ferromagnetism in $\text{Zn}_{1-x}\text{Co}_x\text{O}$: a hybrid density-functional study,” *Physical Review B*, vol. 74, Article ID 144432, 2006.
- [27] N. H. Hong, J. Sakai, N. T. Huong, N. Poirot, and A. Ruyter, “Role of defects in tuning ferromagnetism in diluted magnetic oxide thin films,” *Physical Review B*, vol. 72, no. 4, Article ID 045336, 2005.
- [28] E.-Z. Liu, Y. He, and J. Z. Jiang, “Ferromagnetism induced by defect complex in Co-doped ZnO,” *Applied Physics Letters*, vol. 93, Article ID 132506, 2008.
- [29] C. W. Zhang and S. S. Yan, “Origin of ferromagnetism of Co-doped SnO_2 from first-principles calculations,” *Journal of Applied Physics*, vol. 106, Article ID 063709, 2009.
- [30] X. L. Wang, C. Y. Luan, and Q. Shao, “Effect of the magnetic order on the room-temperature band-gap of Mn-doped ZnO thin films,” *Applied Physics Letters*, vol. 102, Article ID 102112, 2013.

Research Article

Transport, Magnetic, and Thermal Properties of $\text{La}_{0.7}\text{Ca}_{0.24}\text{Sr}_{0.06}\text{MnO}_3$ Single Crystal

Tejas M. Tank,¹ Ashish Bodhaye,² Ya M. Mukovskii,³ and Sankar P. Sanyal¹

¹ Solid State Physics Laboratory, Department of Physics, Barkatullah University, Bhopal 462 026, India

² Department of Physics, St. Vincent Pallotti College of Engineering & Technology, Nagpur 441 108, India

³ Moscow State Steel and Alloys Institute, Moscow 117 936, Russia

Correspondence should be addressed to Tejas M. Tank; tejas.physics2020@gmail.com

Received 13 May 2013; Accepted 16 July 2013

Academic Editor: Shoubao Zhang

Copyright © 2013 Tejas M. Tank et al. This is an open access article distributed under the Creative Commons Attribution License, which permits unrestricted use, distribution, and reproduction in any medium, provided the original work is properly cited.

We report the transport, magnetic, and thermal properties of $\text{La}_{0.7}\text{Ca}_{0.24}\text{Sr}_{0.06}\text{MnO}_3$ single crystal. It was prepared using floating zone technique used under oxygen pressure of 1 bar with a typical growth rate of 1 mm/hr. The resistivity data shows the metal to insulator transition (M-I) occurring at $T_{\text{MI}} = 290$ K along the c -axis and at $T_{\text{MI}} = 280$ K along the ab -plane. It is observed that the T_{MI} is higher along the c -axis as compared to that in the ab -plane, thus indicating that more favorable hopping of electrons is along the c -axis. From bolometric application point of view, the temperature coefficient of resistance (TCR) is found to be $\sim 28\% \text{ K}^{-1}$. The ac -susceptibility measurement shows that this material exhibits ferromagnetic to paramagnetic transition temperature (T_C) 277 K. Sharp peak around this temperature in heat capacity data indicates the onset of long-range ordering. The entropy change associated with this transition is found to be 2.3 J/mol K.

1. Introduction

The colossal magnetoresistance (CMR) of hole doped manganites $\text{RE}_{1-x}\text{A}_x\text{MnO}_3$, with RE = La, Nd, and Pr and A = Ba, Sr, Ca, and Pb, is promising magnetoresistance materials in which the change of resistivity by applying magnetic field is so large that this effect is described as colossal. They were studied very intensively in the last few years due to the effect of CMR [1–4]. They exhibit ferromagnetic to paramagnetic (FM-PM) as well as metal to insulator (M-I) transition. The perovskite structure of ABO_3 with A = La, Pr, and Nd and B = Mn, is paramagnetic insulator at all temperatures. When these are doped with divalent ion, their resistivity decreases with formation of Mn^{+4} , which decreases the Jahn-Teller distortion, creates double exchange interactions, and hence plays a crucial role in the electrical transport and magnetic properties of these oxides [1]. $\text{La}_{1-x}\text{A}_x\text{MnO}_3$ perovskite systems have been studied extensively for their remarkable CMR properties that have technological applications [5]. The CMR behavior occurs near the ferromagnetic (FM) transition

temperature, and this remarkable phenomenon is attributed to the magnetic coupling between Mn^{+3} and Mn^{+4} ions as well as to the strong electron-phonon coupling arising due to Jahn-Teller splitting of Mn $3d$ levels. It has also been found that the bond angle and bond length of $\text{Mn}^{+3}-\text{O}^{2-}-\text{Mn}^{+4}$ play a crucial role in controlling the CMR properties of these manganites as the geometric quantity and the tolerance factor are modified when suitable ions are substituted for La to fill the $3d$ network of MnO_6 octahedra [6]. The problem, however, is that samples used for such studies (typically ceramic, thin films, or single crystal) represent properties of samples but not the compound as such. It concerns especially magnetic and electrical characteristics because they are extremely sensitive to the defect structure of samples. In the case of ceramic and thin film samples, these properties are determined mostly by grain boundaries and the substrate-thin film interface, respectively. The single crystals are more preferable for the right investigations, but manganite crystals of the nominal composition demonstrate significantly different magnetic and electric characteristics

depending on their mosaicity and/or point defect structure. So, preparation of high-quality single crystals of manganite is more important. We have chosen $\text{La}_{0.7}\text{Ca}_{0.24}\text{Sr}_{0.06}\text{MnO}_3$ single crystal as $\text{La}_{0.7}\text{Ca}_{0.3}\text{MnO}_3$ [7] and $\text{La}_{0.7}\text{Sr}_{0.3}\text{MnO}_3$ [8], which exhibit a Curie transition below and above room temperature, respectively. Therefore it is expected that the solid solution between end members, that is, the compounds with $0 < x < 0.33$, might have the Curie temperature in between (i.e., around room temperature), leading to magnetocaloric and magnetoresistive temperature working range relevant to device designed at ambient condition. Earlier, no such efforts have been made, so the present results could not be compared with earlier work.

Among other methods, the floating zone (FZ) method is most suitable for the growth of CMR manganite. In this paper, the transport, magnetic, and thermal properties of $\text{La}_{0.7}\text{Ca}_{0.24}\text{Sr}_{0.06}\text{MnO}_3$ single crystal have been studied.

2. Experimental

The single crystal of $\text{La}_{0.7}\text{Ca}_{0.24}\text{Sr}_{0.06}\text{MnO}_3$ was prepared by using floating zone technique with radioactive heating under oxygen pressure of 1 bar with a typical growth rate of 1 mm/hour. The size of crystal was 4.76 mm in diameter and 3.2 mm in length. Temperature dependence of electrical resistivity was measured using standard four-probe method along ab -plane and c -axis in temperature range 77 K to 300 K. The ac -susceptibility was measured using susceptometer as a function of temperature at 3.87 Oe magnetic field and an exciting frequency of 131.11 Hz. The specific heat was measured by the semiadiabatic heat pulse method. The temperature was varied by using a commercial liquid nitrogen closed cycle cryostat equipped with a temperature controller. All measurements were carried out in the temperature range 80–300 K [9].

3. Results and Discussion

Typical plot of resistivity versus temperature for $\text{La}_{0.7}\text{Ca}_{0.24}\text{Sr}_{0.06}\text{MnO}_3$ single crystal along ab -plane and c -axis is shown in Figure 1. Such a study was undertaken so as to estimate the direction dependence of charge flow. It is seen from Figure 1 that along ab -plane there is a large increase in resistivity (of about five times) as compared to that along c -axis. Such an evolution is a characteristic of an insulator to metal (I-M) transition with decreasing temperature coinciding with an abrupt change of the magnetic state. Here the resistivity shows a peak at 280 K, which separates the high temperature paramagnetic insulating phase from the low temperature ferromagnetic metallic phase. It is noted that the M-I transition temperature is higher and its magnitude is less than that of ab -plane. This is expected, as the Mn–O–Mn bond along c -axis is linear (i.e., 180°), while the same along ab -plane is nonlinear. Thus the hopping of electron is favorable along the c -axis and not in the ab -plane. This can be understood from metal to insulator (M-I) transition at $T_{\text{MI}} = 290$ K along c -axis. The magnitude of resistance along the c -axis is small (of the order of 1Ω).

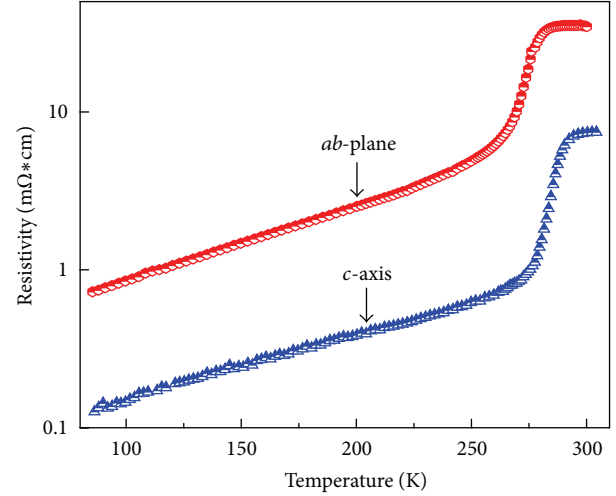


FIGURE 1: Resistivity versus temperature plot for the single crystal of $\text{La}_{0.7}\text{Ca}_{0.24}\text{Sr}_{0.06}\text{MnO}_3$.

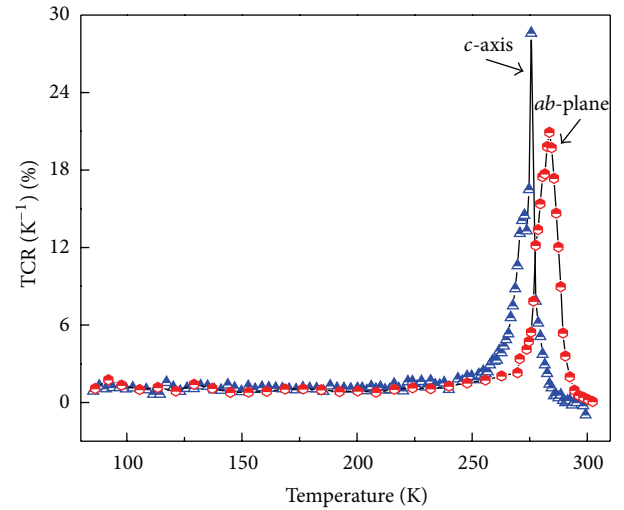


FIGURE 2: TCR versus temperature plot for the single crystal of $\text{La}_{0.7}\text{Ca}_{0.24}\text{Sr}_{0.06}\text{MnO}_3$, along ab -plane and along c -axis.

To evaluate the possibility of this single crystal for sensor application point of view, we have calculated the temperature and the field sensitivity of resistivity. This parameter is quantified in terms of temperature coefficient of resistance (TCR) and is shown in Figure 2.

Consider the following:

$$\left[\text{TCR} = \left(\frac{1}{R} \right) * \left(\frac{dR}{dT} \right) * 100\% \right]. \quad (1)$$

It seems that the maximum TCR value we got along c -axis is $28.6\% \text{ K}^{-1}$ whereas along ab -plane value of TCR is $21\% \text{ K}^{-1}$. This is expected, as the Mn–O–Mn bond along c -axis is linear (i.e., 180°). Such large TCR values are a highly desirable goal in the context of the development of highly responsive bolometer.

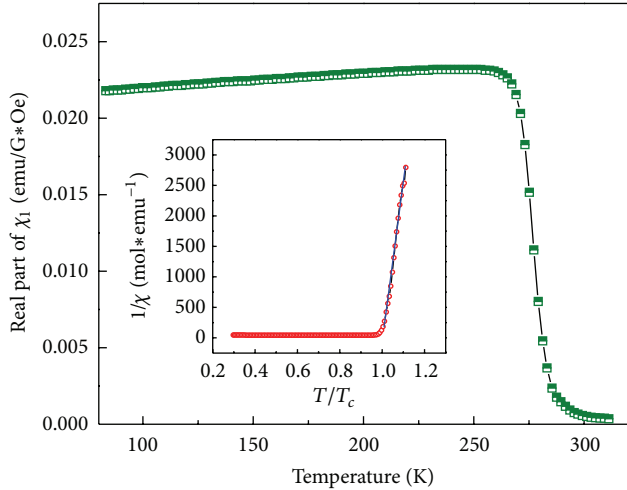


FIGURE 3: Real part of ac -susceptibility for $\text{La}_{0.7}\text{Ca}_{0.24}\text{Sr}_{0.06}\text{MnO}_3$ single crystal.

The temperature dependence of the real part of ac -susceptibility has been measured at fixed applied field of 3.87 Oe and an exciting frequency of 131.1 Hz. This result is shown in Figure 3. The $\text{La}_{0.7}\text{Ca}_{0.24}\text{Sr}_{0.06}\text{MnO}_3$ single crystal undergoes a phase transition from paramagnetic to a ferromagnetic state at the Curie temperature $T_C = 277$ K. Therefore, the magnetic measurement is in good agreement with the resistivity results. Plot shown in the inset is the evidence for short-range ferromagnetic correlations that emerge from the susceptibility measurements. The Curie-Weiss behavior is followed above $1.0 T_C$, but below this temperature the behavior clearly indicates the presence of short-range ferromagnetic correlations which is in good agreement with the resistivity and specific heat results.

The temperature dependence of specific heat of $\text{La}_{0.7}\text{Ca}_{0.24}\text{Sr}_{0.06}\text{MnO}_3$ single crystal is shown in Figure 4. It shows a deviation from the onset ferromagnetic ordering around 276 K, which is close to the transition temperature obtained from the ac -susceptibility and resistivity measurements. A comparison of these data with that of LCMO single crystal [7] shows that by codoping of Sr, we have achieved a larger transition temperature (near the room temperature) which can be useful for device application. This change in the heat capacity data indicates the onset of long-range ordering. To estimate the entropy change associated with the transition, we subtracted the background, which is obtained by fitting the measured heat capacity data excluding peak region with a polynomial. The entropy change associated with this transition is found to be 2.3 J/mol K.

4. Conclusion

All these measurements are consistent with each other to reveal the electronic and magnetic phase transition in CMR single crystal investigated by doping small amount of Sr (0.06%). This study reveals that the magnetic transition temperature increases substantially to 277 K and also matches

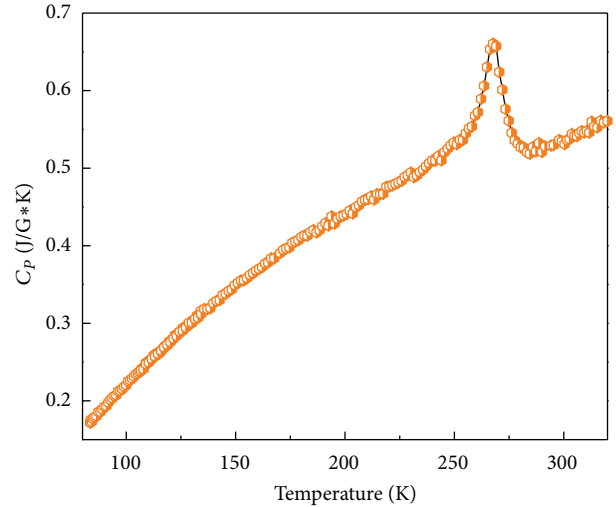


FIGURE 4: Specific heat versus temperature for $\text{La}_{0.7}\text{Ca}_{0.24}\text{Sr}_{0.06}\text{MnO}_3$ single crystal.

with heat capacity data which indicates the onset of long-range ordering around 276 K around room temperature, and large TCR values are a highly desirable goal in the context of the development of highly responsive bolometer device application.

Acknowledgments

The authors are grateful to Dr. A. Banerjee, Dr. R. Rawat, and Dr. G. S. Okram at UGC-DAE-CSR, Indore, India; for providing experimental facilities and UGC (SAP). They are also grateful to Dr. Vilas Shelke, BU, Bhopal, for useful discussion. Tejas M. Tank would like to acknowledge UGC-SAP, New Delhi, India, for award of UGC (SAP)-JRF.

References

- [1] C. N. R. Rao and B. Raveau, *Colossal Magnetoresistance, Charge Ordering and Related Properties and Manganese Oxides*, World Scientific, Singapore, 1st edition, 1998.
- [2] Y. Tokura, *Colossal Magnetoresistive Oxides*, Gordon and Breach Science, Singapore, 1st edition, 2000.
- [3] A. P. Ramirez, "Colossal magnetoresistance," *Journal of Physics Condensed Matter*, vol. 9, no. 39, pp. 8171–8199, 1997.
- [4] A. Urushibara, Y. Moritomo, T. Arima, A. Asamitsu, G. Kido, and Y. Tokura, "Insulator-metal transition and giant magnetoresistance in $\text{La}_{1-x}\text{Sr}_x\text{MnO}_3$," *Physical Review B*, vol. 51, no. 20, pp. 14103–14109, 1995.
- [5] E. O. Wollan and W. C. Koehler, "Neutron diffraction study of the magnetic properties of the series of perovskite-type compounds $[(1-x)\text{La}, x\text{Ca}]\text{MnO}_3$," *Physical Review*, vol. 100, no. 2, pp. 548–575, 1955.
- [6] V. Ravindranath, M. S. Ramachandra Rao, G. Rangarajan et al., "Magnetotransport studies and mechanism of Ho- and Y-doped $\text{La}_{0.7}\text{Ca}_{0.3}\text{MnO}_3$," *Physical Review B*, vol. 63, no. 18, 7 pages, 2001.

- [7] S.-B. Tian, M.-H. Phan, S.-C. Yu, and N. H. Hur, "Magnetocaloric effect in a $\text{La}_{0.7}\text{Ca}_{0.3}\text{MnO}_3$ single crystal," *Physica B*, vol. 327, no. 2–4, pp. 221–224, 2003.
- [8] P. Lin, S. H. Chun, M. B. Salamon, Y. Tomioka, and Y. Tokura, "Magnetic heat capacity in lanthanum manganite single crystals," *Journal of Applied Physics*, vol. 87, no. 9, pp. 5825–5827, 2000.
- [9] A. Bodhaye, S. P. Sanyal, G. S. Okram, and Y. M. Mukovskii, "Transport, magnetic and thermal properties of $\text{La}_{0.88}\text{Ca}_{0.12}\text{MnO}_3$ single crystal," *Indian Journal of Pure and Applied Physics*, vol. 45, no. 1, pp. 37–39, 2007.